VI Escuela
" La Hechicera "
Relatividad, Campos y Astrofísica

Gustavo Bruzual A.
Juan García-Bellido
Esteban Roulet

Universidad de Los Andes
Facultad de Ciencias
Mérida, Venezuela

Noviembre, 2000

Editores:
Héctor Rago — Nelson Pantoja

Diagramación:
Mayerlin Uzcátegui

Portada:
Héctor Acosta

Impresión:
Digital Impresos

"HECHO EL DEPOSITO DE LEY" fl07420005302487
ISBN 980-292-857-7

Escuela "La Hechicera", Relatividad, Campos y Astrofísica

Prefacio

El presente volumen recoge las notas de los cursos impartidos durante la VI Escuela “La Hechicera”, llevada a cabo entre el 05 y el 10 de noviembre del 2000, en la Facultad de Ciencias de la Universidad de Los Andes, Mérida, Venezuela.
La cosmología fue en esta oportunidad el tema central de la escuela y los profesores invitados a dictar los cursos fueron: Gustavo Bruzual A. (Centro de Investigaciones de Astronomía, Venezuela), Juan García-Bellido (Universidad Autónoma Cantoblanco, España) y Esteban Roulet (Universidad Nacional de La Plata, Argentina).

Agradecimientos

Los miembros del comité organizador de la VI Escuela, Alejandra Melfo (Coordinador), Adel Khoudeir, Nelson Pantoja, Héctor Rago (Universidad de Los Andes), Pio Arias (Universidad Central de Venezuela), Willians Barreto (Universidad de Oriente) y Jorge Stephany (Universidad Simón Bolivar), desean expresar su agradecimiento a la Universidad de Los Andes (ULA), al Consejo Nacional de Investigaciones Científicas y Tecnológicas (CONICIT) y a Fundacite Mérida, por el patrocinio y soporte financiero. También agradecemos la invaluable ayuda prestada por Dalia Marquez en todas aquellas cuestiones no científicas vinculadas a la organización de la escuela y a Mayerlin Uzcátegui por la diagramación de este libro.

El Comité Organizador

Índice General

Part III

Lensing phenomena in the Universe

Esteban Roulet

Departamento de Física.
Universidad Nacional de La Plata

CC67, 1900, Argentina.

e-mail: roulet@venus.fisica.unlp.edu.ar

Abstract

In these lectures I discuss two different lensing phenomena which are important in astrophysics. One is that of gravitational lensing of light from distant sources by intervening matter and the other is that of magnetic lensing of charged ultra-high energy cosmic rays by intervening magnetic fields. I discuss the importance of gravitational lensing to learn about the mass distribution of the Universe, to measure the expansion rate H_0, to study the density profiles in clusters, and in particular to study the amount of massive astrophysical compact objects (MACHOs) in our galaxy using microlensing experiments to see how much these contribute to the dark matter present in the galactic halo. Concerning the magnetic lensing, I show that, as in the gravitational case, it can lead to the production of multiple images of a source and to strong enhancement of the fluxes when the source is near a caustic. Since the flux magnification here is energy dependent, it can modify the spectrum of cosmic ray sources. These effects should then be taken into account in the interpretation of the observed events at the highest energies, and can be very important if there is a heavy component in the cosmic rays or even for protons in certain models for the magnetic field of the Galaxy.

Chapter

18

Gravitational lensing

18.1 Historical remarks

The bending of light in a gravitational field predicted by general relativity provided one of the first verifications of Einstein theory. The value of the deflection angle which results, which is twice as large as the one predicted in Newtonian theory, has now been tested at the 0.02% level by observing the change in the apparent position of stars whose light is deflected by the Sun. In 1920, Eddington noted that the light deflection by a stellar object would lead to a secondary dimmer image of a source star on the opposite side of the deflector. Chwolson later pointed out that these secondary images could make foreground stars appear as binaries, and that if the alignment were perfect, the image of the source would be a ring. In 1936, Einstein published the correct formula for the magnification of the two images of a very distant star, and concluded that this lensing effect was of no practical relevance due to the unresolvably small angular separation of the images and the low probability for a high amplification event to take place.

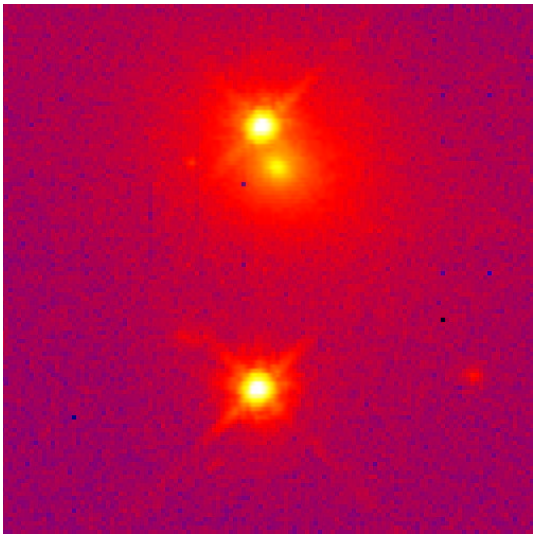

Figure 18.1: HST picture of the first binary quasar observed, QSO0957+561. The angular separation between images is $6.1''$, and the lensing galaxy is close to the image on the top.

The following year, Zwicky showed that, if the deflecting object were a galaxy instead of a single star, the gravitational lensing of the light of a background galaxy would lead to resolvable images. This 'macrolensing' effect would provide information about the mass of the intervening galaxy and allow observation of objects at much larger distances due to the magnification of their light. Furthermore, the probability that this effect be observed becomes practically a 'certainty'.

It was actually the multiple imaging of a high redshift quasar by a foreground galaxy which provided the first observation of gravitational lensing by Walsh et al. in 1979 (see Fig. 18.1), and this area of research has now

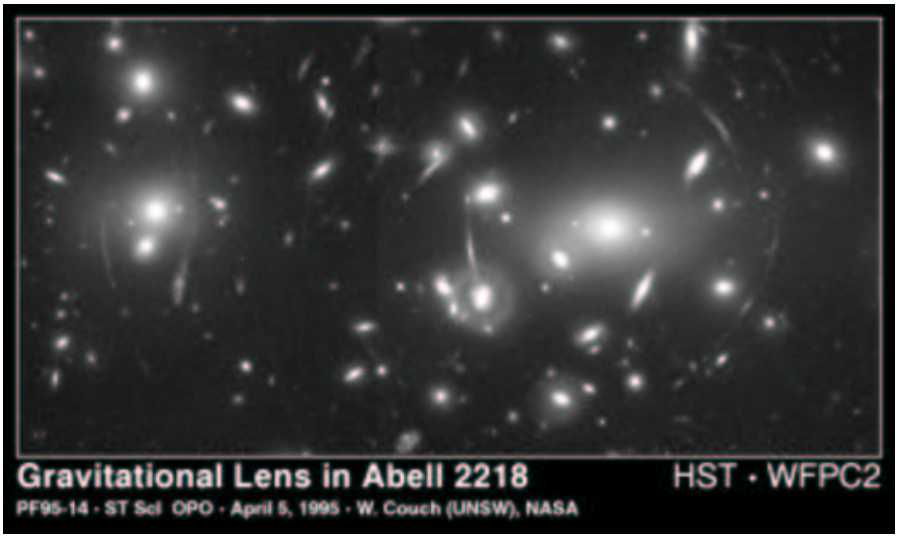

Figure 18.2: Giant arcs around the cluster Abell 2218, produced by the lensing effect of the cluster mass on background galaxies.

become an active field in astronomy, with the potential of giving crucial information for cosmology. For instance, the time delay among the multiple images of a quasar allows one to relate the lens mass, which can be reconstructed from the location and shape of the images, to the Hubble constant, and this procedure is becoming nowadays a competitive way to determine the expansion rate of the Universe.

Another interesting example is that the mass distribution of a cluster can be reconstructed from the shapes of the images of thousands of background faint blue galaxies around it, which become elongated due to the effect of weak lensing by the cluster. In rich clusters of galaxies, strong lensing effects can lead to multiple images of a background galaxy, forming giant arcs around the cluster core, what allows the central cluster mass to be inferred. In this way, the clusters also act as giant lenses ('Zwicky telescopes') magnifying the background galaxies by a large factor, as shown in Fig. 18.2.

The theoretical study of gravitational lensing of stars by stars restarted in 1964, with the work of Liebes and Refsdal, who extended the formalism and discussed the lensing of stars in the disk of the Galaxy, in globular clusters and in the Andromeda galaxy.

The lensing effect of individual stars belonging to a galaxy that is itself macrolensing a background source (see fig. 18.3) was discussed by Chang and Refsdal. When both the lensed source and the intervening galaxy are at cosmological distances, the passage of one of these stars close to the line of sight to one of the images further deflects the source light by an angle which is typically of $\mathcal{O}(\mu\text{arcsec})$. The name 'microlensing' (ML) then became associated with this process, and is now generally applied to any gravitational lensing effect by a compact object producing unresolvable images of a source and potentially huge magnifications of its light.

Press and Gunn showed in 1973 that a cosmological density of massive compact dark objects could manifest through the ML of high redshift sources. In 1981, Gott pointed out the possibility of detecting the dark halos of remote galaxies by looking for ML of background quasars. It was in 1986 that Paczyński noted that, by monitoring the light–curves of millions of stars in the Large Magellanic Cloud (LMC) for more than a year, it should become possible to test whether the halo of our galaxy consisted of compact objects with masses between 10^{-6} and $10^{2}\ M_{\odot}$, i.e. covering most of the range where baryonic dark matter in the form of planets, Jupiters, brown dwarfs or stellar remnants (dead stars, neutron stars or black holes) could lie. It was later realized that the Galactic bulge stars also provided an interesting target to look at, since at least the lensing by faint stars in the disk should grant the

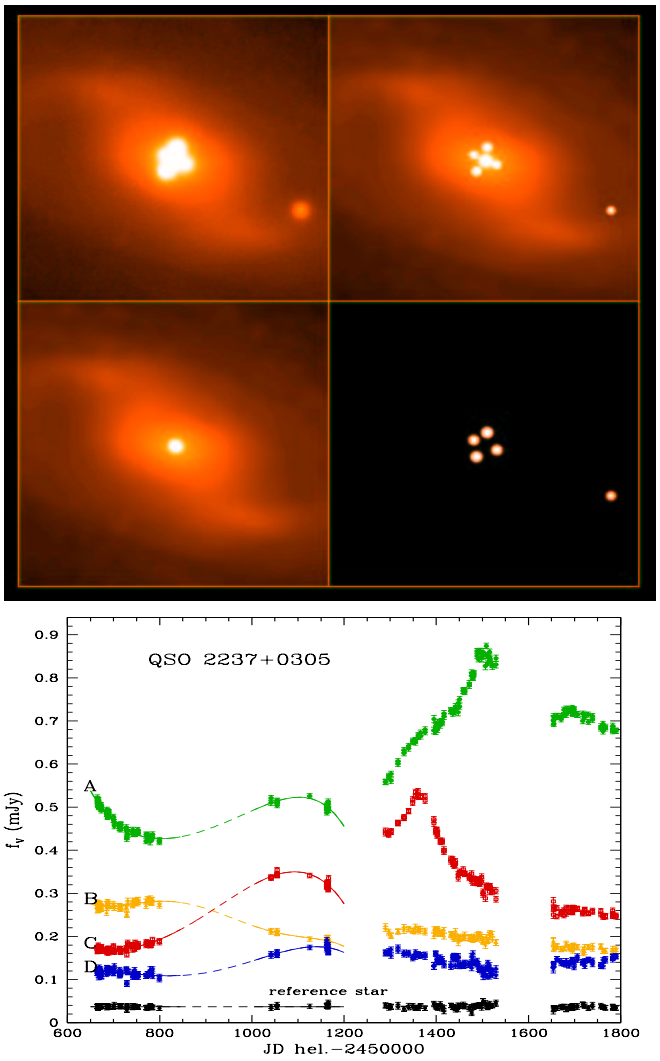

Figure 18.3: Einstein-cross images, which after reduction are separated into the lensing galaxy (bottom left) and the four quasar images (bottom right). The lower panel shows the light-curve of the four images measured by the OGLE collaboration, showing the variations due to microlensing by stars in the bulge of the lensing galaxy.

observation of ML events, and observations in the bulge could also allow one to test the dark constituency of the Galaxy close to the Galactic plane.

Several groups undertook the observations towards the LMC (EROS and MACHO collaborations) and towards the bulge (MACHO and OGLE), obtaining the first harvest of ML events in 1993 (see fig. 18.4). Many follow-up programs are also studying alerted ongoing microlensing events in search of planetary signals or other fine details which could give further information on the lenses. The observations at present are already providing crucial insights into the dark matter problem, into the non–luminous contribution to the mass of the different Galactic components and they are helping to unravel the morphology of the inner part of the Galaxy.

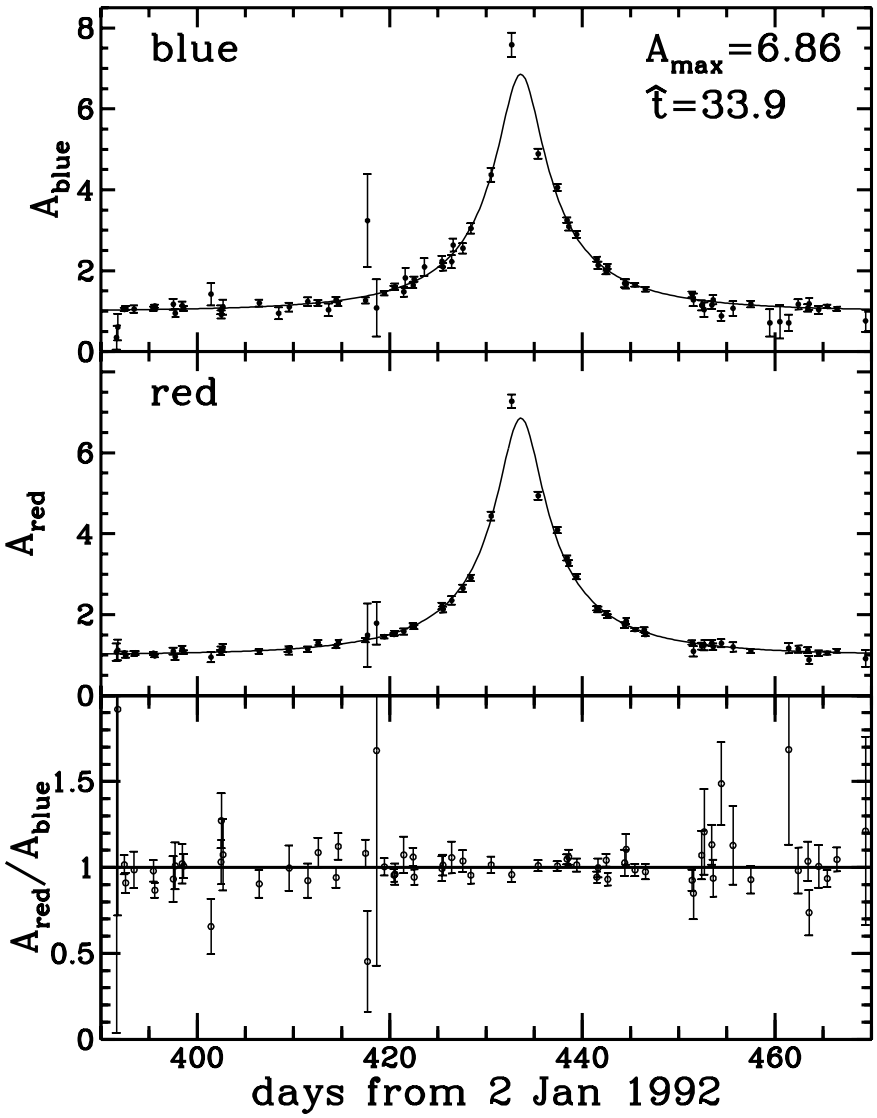

Figure 18.4: Lightcurve of the first microlensing event of a star in the LMC obtained by the MACHO collaboration. The ratio of the lightcurve in two colors is shown in the bottom panel, illustrating the achromaticity of this gravitational effect.

18.2 The dark matter problem

One of the main applications of gravitational lensing is to use it to measure the amount of mass in the Universe and in particular to understand the nature of the dark matter, which is one of the pressing unsolved mysteries in cosmology and particle physics nowadays. The dark matter problem is the fact that the matter in luminous forms (stars and gas) is inferred to account only for $\Omega_{lum} \simeq 0.007$, i.e. for less than one percent of the critical density. On the other hand, dynamical estimates based on the gravitational influence of the mass on test bodies (gas orbiting galaxies, galaxies moving inside clusters) imply that there is at least ten times more 'dark' mass than luminous one on galactic scales, and even more ($\Omega \sim 0.3$) on cluster scales. On cluster scales the evidence comes not only from virial estimates using the observed galaxy motions, but also from the reconstruction of the gravitational potential from the observed X-ray temperature profiles, assuming that the hot gas in the cluster is in hydrostatic

equilibrium, and also (what is more important for us here) from the gravitational effects of the clusters on the light from background sources[1]. The issue on even larger scales is still unsettled, existing at present indications in favor of some dark energy (cosmological constant) accounting for $\Omega_\Lambda \simeq 0.7$, i.e. filling the gap up to the inflation preferred value $\Omega = 1$ corresponding to a flat universe.

The possible constituents of the dark matter naturally split into baryonic and non-baryonic candidates. The last ones would be some kind of weakly interacting particle permeating the universe, such as supersymmetric neutralinos, axions or massive neutrinos, while the first ones would be made of just ordinary protons and neutrons hidden in some non-luminous forms. The simplest examples to achieve this would be to have them in MACHOs (the acronym for massive astrophysical compact halo objects), such as stellar remnants (white dwarfs, neutron stars, black holes), brown dwarfs (stars with mass $m < 0.1 M_\odot$, which never become hot enough to start sustained nuclear fusion reactions) or even planets. Although dark compact objects are, by definition, very hard to be seen directly, they may reveal themselves through the gravitational lensing effect they produce on background stars. Also cold gas clouds could naturally constitute baryonic dark matter.

The main constraints on the amount of baryons in the universe come from the theory of primordial nucleosynthesis, which requires $\Omega_b \simeq 0.01 - -0.05/(H_0/70 km/s/Mpc)^2$, with the lower (higher) values corresponding to the high (low) primordial deuterium abundance determinations from QSO absorption lines [1]. Hence, we see that for a Hubble constant $H_0 \simeq 50$–70 km/s/Mpc nucleosynthesis indicates that dark baryons should exist and that their total amount is probably insufficient to account for dark galactic halos ($\Omega \simeq 0.1$). Clearly to account for the observations on cluster scales non-baryonic dark matter is also required, and it would then be natural to expect to have some amount of it also at galactic scales.

We will now discuss the basic gravitational lensing formalism and present the main results of macro- and micro-lensing observations.

18.3 Gravitational lensing formalism

When a light ray passes close to a compact object of mass m, it is deflected according to general relativity by an angle

$$\hat{\alpha} = \frac{4Gm}{c^2 \xi}, \tag{18.1}$$

where ξ is the impact parameter between the light ray trajectory and the deflector. When the deflector is an extended object, like a galaxy or a cluster, or if it consists of more than one point-like lens, such as in a binary system, the total deflection is obtained as the sum of the deflections produced by each mass element. If the extension of the mass distribution along the line of sight is small compared to the distances between the lens and the observer and between the lens and the source, it is a good approximation to consider just the projected mass in a plane perpendicular to the line of sight, i.e. the so-called lens plane (see Fig. 18.5). In this case the vectorial deflection angle becomes

$$\vec{\hat{\alpha}}(\vec{\xi}) = \frac{4G}{c^2} \int d^2\xi' \frac{\Sigma(\vec{\xi}') \left(\vec{\xi} - \vec{\xi}'\right)}{|\vec{\xi} - \vec{\xi}'|^2}, \tag{18.2}$$

where $\Sigma(\vec{\xi}) = \int \mathrm{d}z \rho(\vec{\xi}, z)$.

It is useful to write the deflection angle in terms of the projected gravitational potential

$$\psi(\vec{\xi}) \equiv \int dz \varphi(\vec{\xi}, z), \tag{18.3}$$

[1]These three methods give results in reasonable agreement when the assumption that the system is relaxed holds and accurate lens models are adopted.

which using the Poisson equation can be related to the surface mass density distribution through

$$\nabla^2_{\vec{\xi}}\psi(\vec{\xi}) = 4\pi G\Sigma(\vec{\xi}). \tag{18.4}$$

Furthermore, recalling that the Green function $\mathcal{G}$ for the two - dimensional Laplacian (satisfying $\nabla^2_{\vec{\xi}}\mathcal{G}(\vec{\xi},\vec{\xi'}) = 2\pi\delta^2(\vec{\xi}-\vec{\xi'})$), is given by $\mathcal{G}(\vec{\xi},\vec{\xi'}) = \ln|\vec{\xi}-\vec{\xi'}|$, the projected potential can be written as

$$\psi(\vec{\xi}) = 2G\int d^2\xi'\Sigma(\vec{\xi'})\ln|\vec{\xi}-\vec{\xi'}|. \tag{18.5}$$

The deflection angle (see Eq. (18.2)) thus turns out to be proportional to the gradient of the projected gravitational potential

$$\vec{\hat{\alpha}}(\vec{\xi}) = \frac{2}{c^2}\vec{\nabla}_{\xi}\psi(\vec{\xi}). \tag{18.6}$$

The lens equation relates the observed angle of an image ($\vec{\theta}$) to the actual position of the source ($\vec{\beta}$), and reads

$$\vec{\beta} = \vec{\theta} - \vec{\alpha}, \tag{18.7}$$

where $\vec{\alpha} \equiv \vec{\hat{\alpha}}D_{LS}/D_{OS}$ and $\vec{\theta} \equiv \vec{\xi}/D_{OL}$.
Let us now introduce a rescaled projected gravitational potential

$$\Psi \equiv \frac{2}{c^2}\frac{D_{LS}}{D_{OS}D_{OL}}\psi. \tag{18.8}$$

Using Eq. (18.6) one has then that $\vec{\alpha} = \vec{\nabla}_{\theta}\Psi$, where the gradient here is taken with respect to the angular variables, and hence the lens equation becomes

$$\vec{\beta} = \vec{\theta} - \vec{\nabla}_{\theta}\Psi(\vec{\theta}). \tag{18.9}$$

For each image position $\vec{\theta}$ there is clearly a unique source position $\vec{\beta}$. However, since the equation is non-linear in $\vec{\theta}$, for some source positions it might be possible to find multiple solutions $\vec{\theta}$ of the lens equation. This would correspond to the formation of multiple images and to the regime which is known as strong lensing.

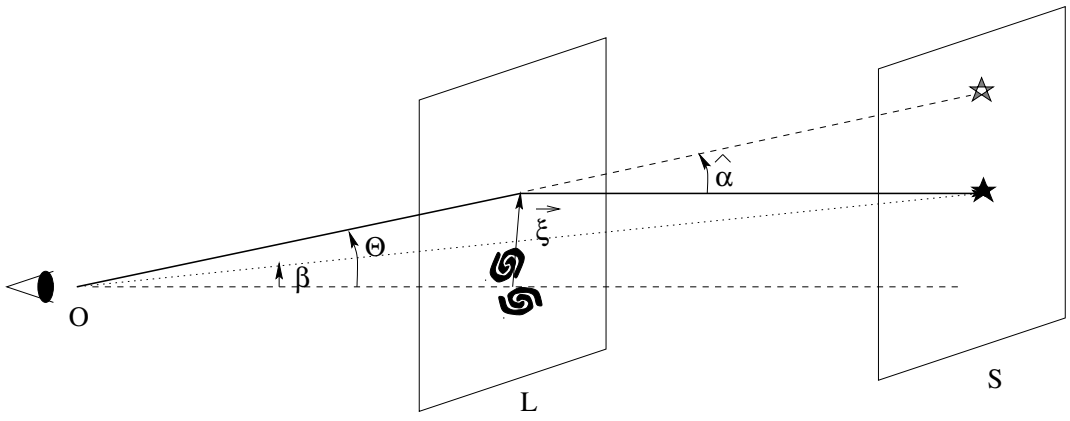

Figure 18.5: Extended lensing distribution.

One can relate a differential element of solid angle in the image plane $d\Omega = d\vec{\theta_1} \wedge d\vec{\theta_2}$ with the corresponding one in the source plane $d\Omega_0 = d\vec{\beta}_1 \wedge d\vec{\beta}_2$, through $d\Omega = J^{-1}d\Omega_0$, where J is the Jacobian of the mapping $\vec{\beta}(\vec{\theta})$, i.e.

$$J = \det\frac{\partial\vec{\beta}}{\partial\vec{\theta}}, \tag{18.10}$$

Since the surface brightness of the source, which is the flux per unit solid angle, is conserved along the light ray trajectory (this is a consequence of Liouville's theorem), the magnification of the corresponding image will just be the ratio of the two solid angles (the actual one and the one that would be observed in the absence of lenses), and is then given by

$$A = \frac{\mathrm{d}\Omega}{\mathrm{d}\Omega_0} = J^{-1}. \tag{18.11}$$

From Eq. (18.9) we can write the matrix of the mapping between the angular coordinates as

$$\mathcal{T}_{ij} \equiv \frac{\partial \beta_i}{\partial \theta_j} = \left(\delta_{ij} - \frac{\partial^2 \Psi}{\partial \theta_i \partial \theta_j}\right). \tag{18.12}$$

It differs from the identity by the Hessian of the rescaled projected gravitational potential Ψ. From the Poisson equation one can see that the Laplacian of Ψ is proportional to the surface density $\Sigma(\vec{\theta})$, and hence we can write

$$\mathrm{Tr}\,\frac{\partial^2 \Psi}{\partial \theta_i \partial \theta_j} = \nabla^2_{\vec{\theta}} \Psi = 2\frac{\Sigma(\vec{\theta})}{\Sigma_c} \equiv 2\kappa(\vec{\theta}), \tag{18.13}$$

where we have defined the critical density $\Sigma_c \equiv c^2 D_{OS}/(4\pi G D_{OL} D_{LS})$ and the convergence $\kappa(\vec{\theta}) \equiv \Sigma(\vec{\theta})/\Sigma_c$. Two additional independent combinations of the second derivatives of Ψ can be defined through

$$\begin{aligned} \gamma_1 &= \frac{1}{2}\left(\frac{\partial^2 \Psi}{\partial \theta_1^2} - \frac{\partial^2 \Psi}{\partial \theta_2^2}\right), \\ \gamma_2 &= \frac{\partial^2 \Psi}{\partial \theta_1 \partial \theta_2} = \frac{\partial^2 \Psi}{\partial \theta_2 \partial \theta_1}. \end{aligned} \tag{18.14}$$

The matrix of the mapping can then be rewritten as

$$\mathcal{T} = \begin{pmatrix} 1-\kappa-\gamma_1 & -\gamma_2 \\ -\gamma_2 & 1-\kappa+\gamma_1 \end{pmatrix}. \tag{18.15}$$

Both γ_1 and γ_2 (as well as κ) are functions of $\vec{\theta}$. The effect of the convergence κ is clearly to change the size of the image of a source without modifying its shape. The part of the matrix formed by the γ_1 and γ_2 terms, called the shear, is the one responsible for the distortions in the image shape. The amplification is given by

$$A = (\det \mathcal{T})^{-1} = \frac{1}{(1-\kappa)^2 - \gamma^2}, \tag{18.16}$$

where we have defined the modulus of the shear, $\gamma \equiv \sqrt{\gamma_1^2 + \gamma_2^2}$. The amplification has then a term coming from an isotropic focusing due to the local matter density in the lens plane, described by κ, and an anisotropic focusing due to the tidal gravitational effects, described by the shear, which leads to a deformation of the image.

The mapping matrix has eigenvalues $1-\kappa-\gamma$ and $1-\kappa+\gamma$. In a coordinate system coinciding with the principal axes of the shear at $\vec{\theta}$, $\mathcal{T}$ is diagonal, and has these eigenvalues in the diagonal. Thus, the image is stretched by a factor $(1-\kappa-\gamma)^{-1}$ in one direction and by $(1-\kappa+\gamma)^{-1}$ in the other. A negative value of one of the factors (negative partial parity) means that the image is inverted in that direction. When both eigenvalues are negative, the total parity of the image is positive and hence it will not be inverted.

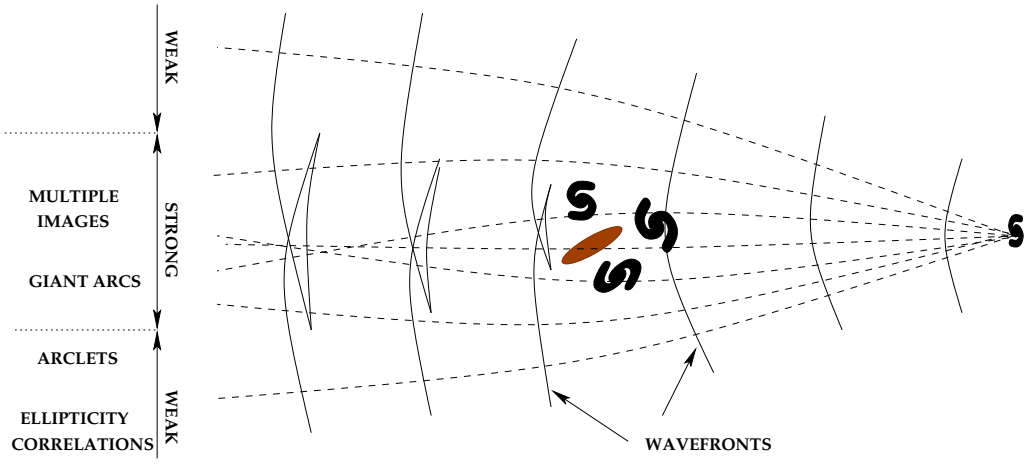

Figure 18.6: Schematic picture of the different macrolensing regimes. The wavefronts of light are displayed as they traverse a lensing distribution. In the central parts multiple images form (strong lensing), while farther from the lens only coherent distortions of the image shapes are observed (weak lensing).

18.4 Gravitational macrolensing

We will now discuss the main observational manifestations of gravitational lensing due to the big structures in the Universe (for reviews see [2, 3]). Figure 18.6 qualitatively illustrates the trajectories of the light rays from a faraway source and crossing a matter distribution.

If the lens is sufficiently massive (typically if $\Sigma > \Sigma_{cr} \simeq 1.66 \times 10^3 M_\odot/\ \mathrm{pc}^2 (D_{OS} Gpc/D_{OL} D_{LS})$), multiple images will form when the background sources are closely aligned with the center of the lensing mass, what will correspond to the different wavefronts arriving to the observer in the central part of the figure. When the potential of the lens mass is non-singular, the extra images of the source always appear in pairs, having opposite parities, what corresponds to the folds observed in the wavefront (each fold adds a pair of images). In this case the total number of images is expected to be odd.

In the regime of strong lensing, giant arcs will be formed if the sources are extended. They appear in the locations where the magnification ($A = 1/((1-\kappa)^2 - \gamma^2)$) is very large, i.e. for $1 - \kappa \simeq \gamma$. For spherical lenses one can show that the total mass contained within the arcs is

$$M(\theta_{arc}) = \Sigma_{cr} \pi (D_{OL} \theta_{arc})^2 \simeq 1.1 \times 10^{14} M_\odot \frac{D_{OL} D_{OS}}{\mathrm{Gpc} D_{LS}}, \tag{18.17}$$

and this gives a rough idea of the mass inside the arcs of a more general lens model.

Hence, the observation of arcs gives crucial information on the central mass of clusters. In general, the odd image number theorem is difficult to test because one of the images is usually near the center of the mass distribution (where bright galaxies are encountered) and appears very demagnified (since there $\kappa \gg 1$), so that it can hardly be seen. This central image actually fades away in the limit in which the mass distribution becomes singular, and is hence absent in particular for the case of compact lenses.

Figure 18.7 shows one of the most beautiful examples of strong lensing. In this HST photo of Cl0024+1654, eight images of the same background galaxy are observed. Requiring that the lens model reproduces the detailed features of all the images, very precise reconstructions of the mass distribution have been obtained [5], showing that in addition to the mass associated to the observed galaxies in the cluster, a smooth and quite symmetric distribution

Figure 18.7: Strong lensing of a background blue galaxy by cluster CL0024+1654 (credit of W. N. Colley, E. Turner and J. A. Tyson [4]). Up to eight images of the same galaxy are seen in this HST photo.

of dark matter is present, with a mass within $107h^{-1}$ kpc (corresponding to the location of the arcs) of

$$M_{107} = 1.662 \pm 0.002 \times 10^{14} h^{-1} \left(\frac{D_{LS}/D_{OS}}{0.57} \right)^{-1} M_{\odot}.$$

The observation of one central image also requires the presence of a soft core of $35h^{-1}$ kpc, and hence is in contrast to some popular density profiles inferred from dark matter simulations of structure formation (Navarro, Frenk and White profiles), although outside the core the agreement is excellent.

Looking now in the region outside the giant arcs, we enter the regime of weak lensing (where $\kappa < 1 - \gamma$ so that no multiple images are formed). To measure the effects of the convergence κ is not easy, because the absolute luminosities of the sources are not known. However, the shear induces a tangential deformation of the images, since it stretches them by a factor $1/(1 - \kappa + \gamma)$ in one direction and $1/(1 - \kappa - \gamma)$ in the orthogonal one. The average ellipticity is then $\langle \epsilon \rangle = \gamma/(1-\kappa)$. For $\kappa \ll 1$ the measured ellipticities of the background sources give then a measure of the shear. Since the shear and the convergence are related both to second derivatives of the potential Ψ, there is an inversion technique (due to Kaiser and Squires [6]) which allows to reconstruct κ from the measured ellipticities, and hence obtain the mass distribution $\Sigma(\vec{\theta}) = \kappa(\vec{\theta})\Sigma_{cr}$. This method applied to CL0024+1654 indeed allows to reconstruct the cluster mass up to distances of ~ 1.5 Mpc from the center, as shown in figure 18.8.

Another very interesting recent development has been the measurement of 'cosmological shear' (see figure 18.9),

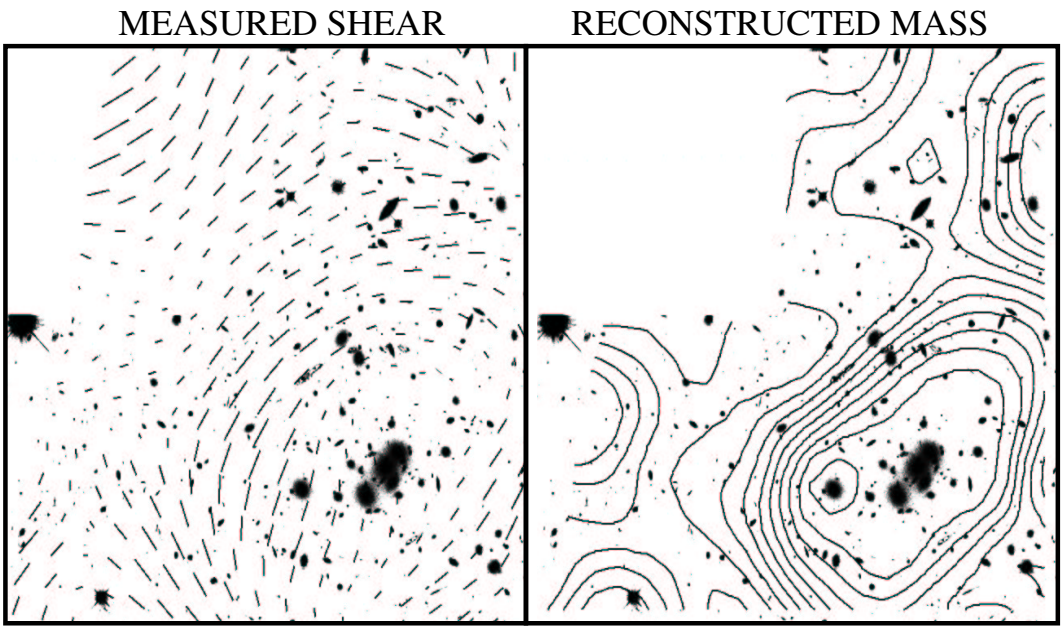

Figure 18.8: Weak lensing around cluster CL0024+1654. On the left is the measured shear field (Mellier and Fort) overlaid in an HST photo, and on the right the reconstructed mass density (Seitz et al.).

i.e. the correlation among galaxy ellipticities in empty fields, far away from known clusters. These ellipticities are produced by the large scale structures predicted in structure formation scenarios and they are correlated typically up to an angular extent of a few tens of arcmin. The signal is small (less than a percent), and the galaxies are themselves intrinsically elliptical so that many have to be averaged in order to obtain the shear induced ellipticity. Hundreds of thousands of galaxy ellipticities need then to be carefully measured to compute the angular correlations between nearby ellipticities. Since the predictions are different in different cosmological scenarios, these results can put important constraints on parameters such as Ω_m or Λ, and strong efforts are being devoted to improve the measures.

Turning now to the lensing of high redshift quasars by galaxies, as we already showed in the optical photo in figure 18.1 and 18.3 it leads to multiple images with typical arcsec separations. When the quasar is radio loud, it is possible to make detailed VLBI maps of the images. This is shown in figure 18.10 for the same famous quasar of Fig. 18.1, where now at milliarcsec resolution it is possible to identify in the two images the core of the quasar and also a jet structure. It is also apparent that the parities of the two images are opposite. Using these images, it is possible to perform detailed mass models for the lens, which have to include the galaxy ellipticity as well as an external shear due to the cluster hosting the lens galaxy.

Finally, let us mention another very important application of quasar lensing, which is the measurement of the expansion rate of the Universe. This comes about because one has the angular information on the image location and the redshifts of the lens and source, but to know the actual length scale of the system would require the knowledge of the Hubble rate H_0. Reversing the argument, if one were able to measure the length scale of the lens, it would be possible to infer the value of H_0 [10]. This is possible if the source is a variable quasar, since in this case the time delay between the two images (which typically ranges between a few days and a few years) can be measured, and sets the scale of the problem. Figure 18.11 shows how the measured light curves of the two images of QSO0957+561 can be used to obtain the time delay, and the analysis of this particular system using very sofisticated mass models for the lens implies that $H_0 = 77^{+29}_{-24}$km/s/Mpc [11]. It is remarkable that these kind of determinations of H_0 are becoming competitive with the other standard ones, and are even starting now to be

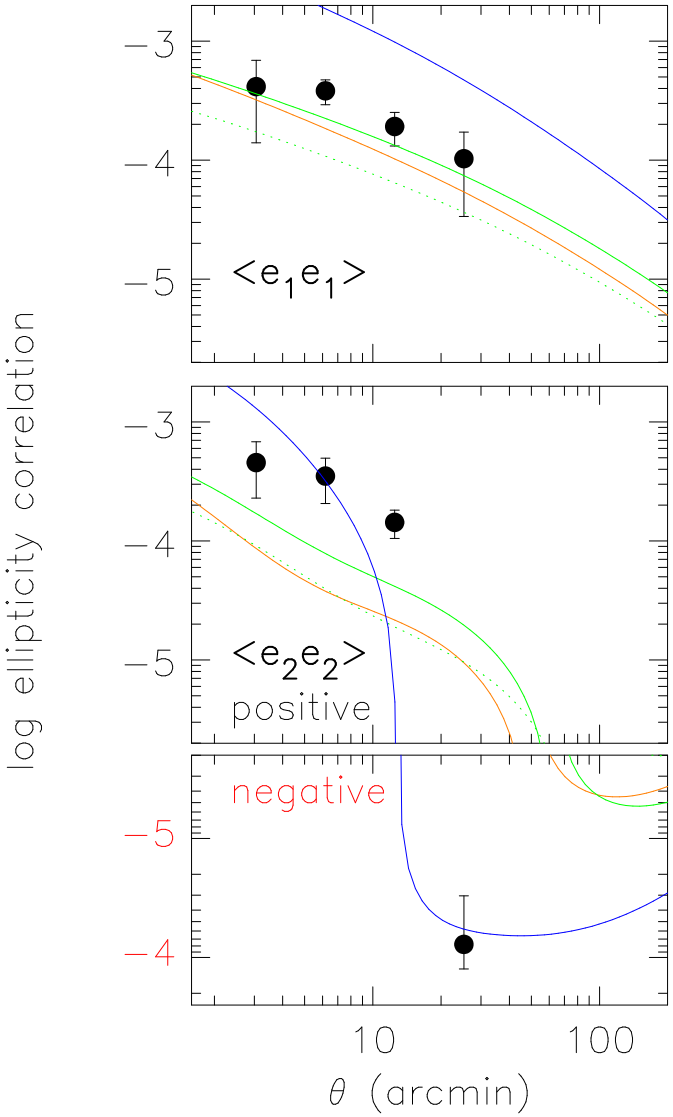

Figure 18.9: Recent measurement of galactic ellipticity correlations in empty fields (without clusters) due to weak gravitational lensing by the large scale structure [7]. Also the predictions for different cosmological models are displayed.

included in the Review of Particle Properties.

18.5 Microlensing in the Local Group

Let us now consider the gravitational deflection of light by a compact object (for reviews see [12, 13]). The geometry of the process in the plane containing the observer, lens and source star, is shown in Fig. 18.12. The light deflection leads to the appearance of a secondary fainter image on the opposite side of the lensing object and also to a lensing effect on the source light.

Let $\theta_\pm$ be the angles of the two source images with respect to the observer–lens line of sight, and β be the angle to

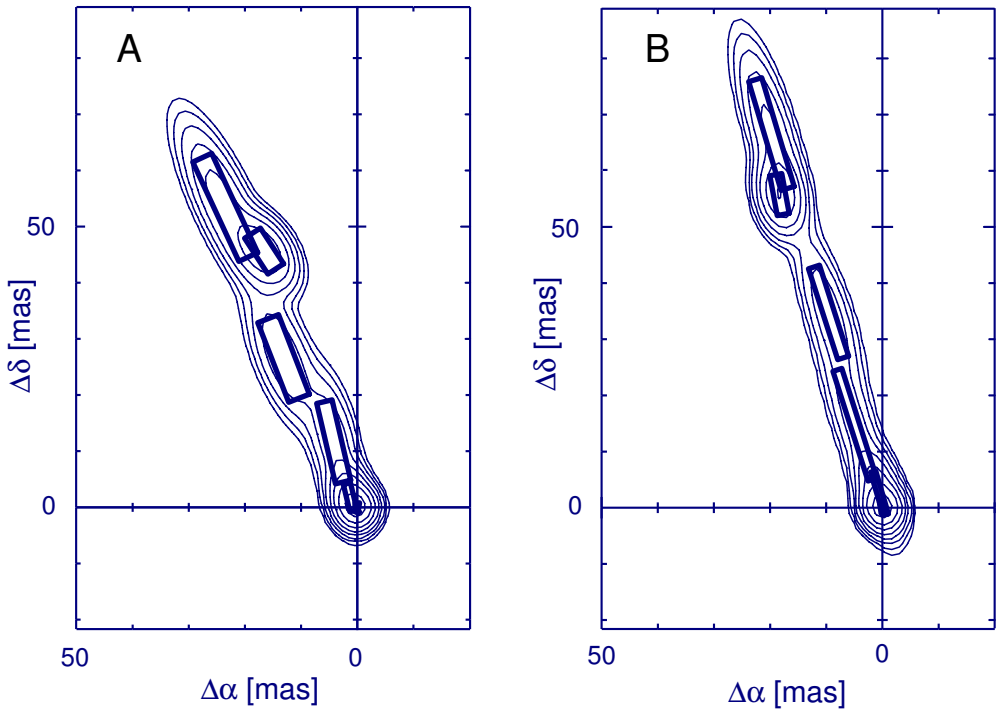

Figure 18.10: VLBI radio map of QSO0957+561. Images A and B show the central radio source and a jet. The rectangles represent the axes and position angles of individual flux components, which are seen in both images and also show that their parities are different (from ref. [8]).

the actual source position. Using that $D_{OS}(\theta_\pm - \beta) = D_{LS}\hat{\alpha}_\pm$, with $\theta_\pm = \xi_\pm / D_{OL}$, it is easy to obtain that

$$\theta_\pm = \frac{1}{2}\left[\beta \pm \sqrt{\left(\frac{2R_E}{D_{OL}}\right)^2 + \beta^2}\right]. \tag{18.18}$$

The Einstein radius

$$R_E \equiv 2\sqrt{\frac{GmD_{OL}D_{LS}}{c^2 D_{OS}}} \tag{18.19}$$

characterizes the size of the impact parameters for which the lensing effect is large, and numerically turns out to be

$$R_E = 9.0 \text{ AU} \sqrt{\frac{D_{OS}}{10 \text{ kpc}} \frac{m}{M_\odot} x(1-x)}, \tag{18.20}$$

where we have introduced the variable $x \equiv D_{OL}/D_{OS}$.

For perfect alignment, $\beta = 0$, the image will actually be a ring, the so–called Einstein ring, centered around the source position and of size $\theta_E = R_E/D_{OL}$. Note that R_E is just the radius of the projection of this ring onto the lens plane (a plane containing the lens and orthogonal to the l.o.s.).

In general, the angular separation between the two images is

$$\Delta\theta \equiv \theta_+ - \theta_- = \sqrt{\left(\frac{2R_E}{D_{OL}}\right)^2 + \beta^2}. \tag{18.21}$$

For impact parameters smaller than R_E one then has

$$\Delta\theta \simeq 1.8\sqrt{\frac{(1-x)}{x}\frac{10 \text{ kpc}}{D_{OS}}\frac{m}{M_\odot}} \text{ mas}. \tag{18.22}$$

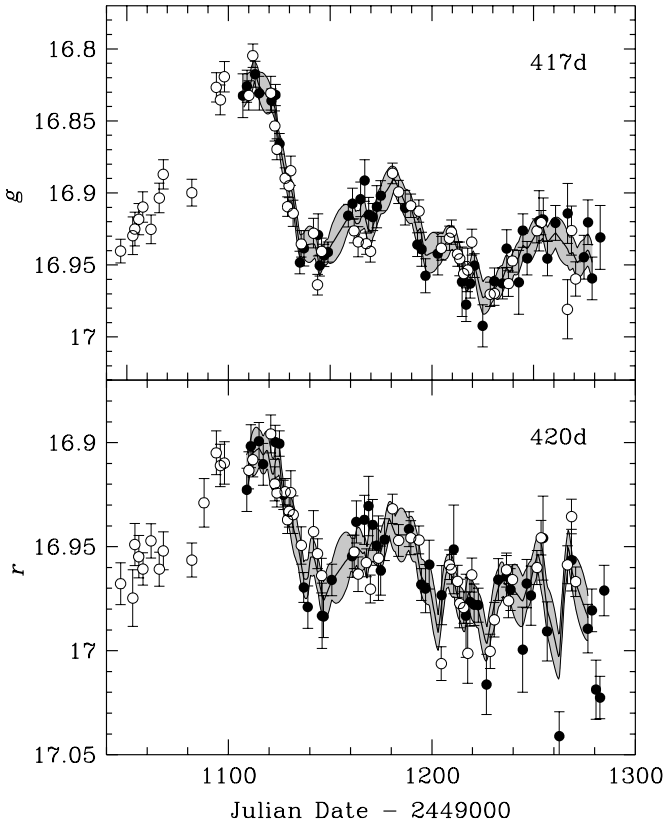

Figure 18.11: Optical light curves in two bands of the two images of QSO0957+561 [9]. Image A (black dots), which is the one closer to the bottom in fig. 18.1, has been displaced temporally in order that the main features of the two images agree. The resulting time delay is ~ 417 days.

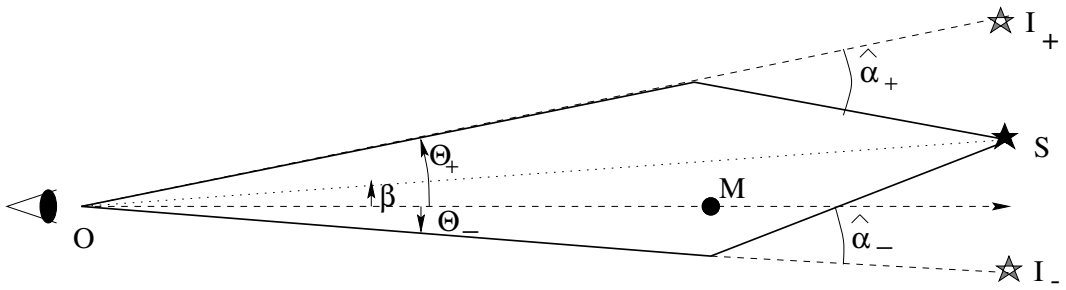

Figure 18.12: Geometry of the deflection of light.

This angle is then of order 1 mas (milliarcsec) for microlensing observations of LMC stars, and $O(\mu\text{as})$ for lenses and sources at cosmological distances ($\gg$ Mpc), as in the case of quasar microlensing by stars in foreground

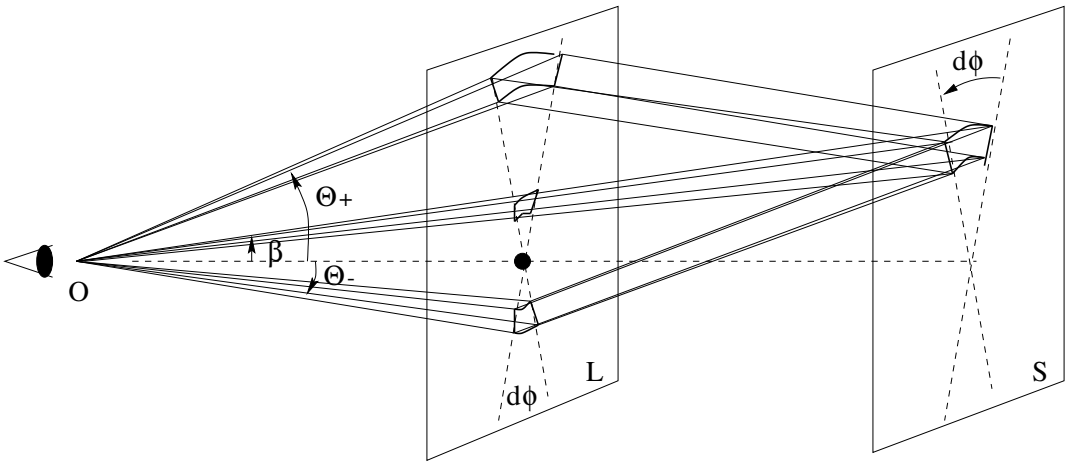

Figure 18.13: Solid angles subtended by the source and its images.

galaxies. Clearly these angular separations are unresolvable with present day telescopes.
The signal which can however be observed as a result of the ML process is the variation of the intensity of the light source due to the motion of the lensing object with respect to the l.o.s. to the source star. The resulting amplification of the light of the source is obtained from the ratio of the solid angles subtended by the source image ($d\Omega_\pm \equiv dS_\pm/(4\pi D_{OL}^2)$) with its value ($d\Omega_0 \equiv dS/(4\pi D_{OS}^2)$) in the absence of lensing effects (see Fig. 18.13). The amplification of the light intensity for each image, A_i, is then

$$A_\pm = \frac{d\Omega_\pm}{d\Omega_0} = \frac{\theta_\pm d\phi d\theta_\pm}{\beta d\phi d\beta}. \tag{18.23}$$

Substituting $d\theta_\pm/d\beta = (1 \pm \beta/\Delta\theta)/2$ leads to a total amplification

$$A \equiv |A_+| + |A_-| = \frac{1}{2}\left[\frac{\beta}{\Delta\theta} + \frac{\Delta\theta}{\beta}\right]. \tag{18.24}$$

Let us define $u \equiv \beta D_{OL}/R_E$ as the distance of the lens to the l.o.s. to the star in units of R_E. We then obtain for the amplification

$$A = \frac{u^2+2}{u\sqrt{u^2+4}}. \tag{18.25}$$

Assuming that the lens moves with constant velocity with respect to the l.o.s. during the duration of the ML event, one has

$$u^2(t) = \frac{b^2 + [v^\perp(t-t_0)]^2}{R_E^2} \equiv u_{min}^2 + \left[\frac{(t-t_0)}{T}\right]^2, \tag{18.26}$$

where b is the minimum distance between the lens trajectory and the l.o.s. to the star, $u_{min} \equiv b/R_E$, t_0 is the time of closest approach and $v^\perp$ is the component of the lens velocity relative to the l.o.s. in the direction perpendicular to this same line. The event duration is defined as

$$T \equiv \frac{R_E}{v^\perp}. \tag{18.27}$$

Combining the expression for $u(t)$ with Eq. (18.25) leads to a time dependent amplification of the luminosity of the source described by a very characteristic light–curve, plotted in Fig. 18.14. Notice that the event duration grows

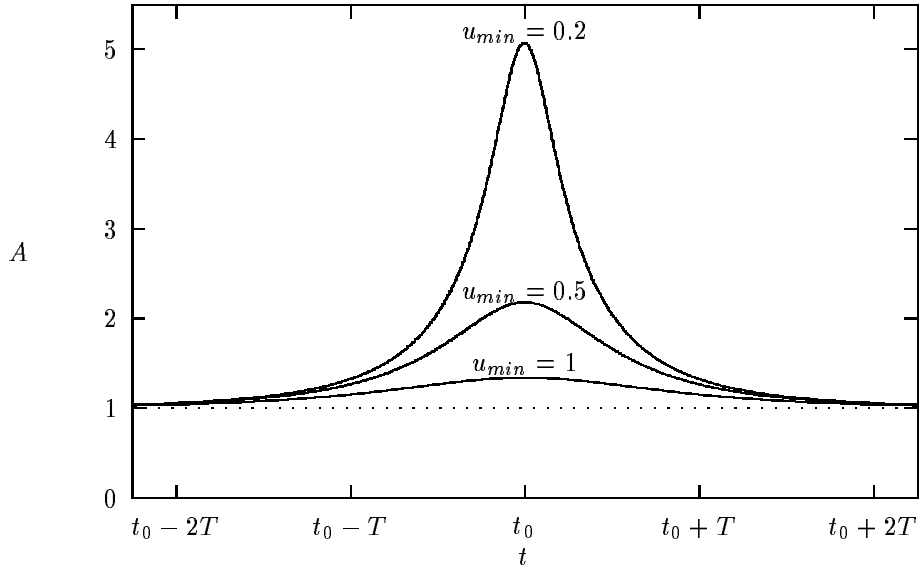

Figure 18.14: Light curve for different impact parameters.

with the mass as $T \propto \sqrt{M}$, but it also depends on the relative velocity of the lens and on the distances to the lens and the source.
The event duration T is determined, together with u_{min} (or equivalently A_{max}) and t_0, by fitting the theoretical light–curve to the observed star luminosities plotted as a function of time. Finally, a crucial characteristic of the ML light–curve is that it should be achromatic, due to the gravitational origin of the lensing effect which causes all wavelengths to be affected equally.

18.5.1 Microlensing expectations

One can estimate the optical depth, i.e. the probability that a given star is magnified significantly for a given lens distribution with number density n_ℓ, as the number of lenses within a distance R_E from the l.o.s.. If the lenses are assumed to have a common mass m, one has $n_\ell = \rho_\ell/m$, and hence

$$\tau = 4\pi \int_0^{D_{os}} \mathrm{d}D_{o\ell}\, R_E^2 n_\ell = \frac{4\pi G D_{os}^2}{c^2} \int_0^1 \mathrm{d}x x(1-x)\rho_\ell.$$

This last equality is actually independent of the lens mass, and hence is also valid for a general lens mass distribution. In the case of a halo consisting fully of MACHOs, the lens density will be just the halo density, which from the observed rotation curve of the Galaxy should be

$$\rho_H \simeq \rho_0^H \frac{r_0^2 + a^2}{r^2 + a^2},$$

where $r_0 = 8.5$ kpc is the distance to the galactic center, the core radius a is of a few kpc and the local halo density is $\rho_0^H \simeq 10^{-2} M_\odot/\mathrm{pc}^3$. This would lead to a predicted optical depth for LMC stars of $\tau^H \simeq 4 \times 10^{-7}$.

The timescale of the events has an average value $\langle T\rangle \simeq 65\mathrm{d}\sqrt{m/M_\odot}$ given the typical velocity dispersion expected for halo objects ($\sigma \simeq 155$ km/s). One can show then that for 100% efficient searches the number of expected events is $N = (2/\pi)(\tau/\langle T\rangle) \times \text{Exposure} \simeq 20 \text{ events}\sqrt{M_\odot/m}(\text{Exposure}/\ 10^7 \text{ stars yr})$. This is what prompted Paczynsky [14] to suggest that following the light curves of a few million stars during a few years would allow to test whether the galactic halo is made of compact objects with masses between 10^{-6} and $10^2 M_\odot$.

Actually, the efficiencies are $\leq 30\%$ and are time dependent, so that a detailed prediction requires to convolute the differential rates with the efficiencies (and also with the mass distribution of the lenses).

18.5.2 First microlensing results and their interpretation

By 1992 the observational searches towards the LMC by the french EROS and australo-american MACHO collaborations had started and already after one year the first candidate events had showed up. It soon became apparent however that the number of events observed were a factor ~ 5 below the expectations from a halo made of objects lighter than a few solar masses. The estimate of the optical depth to the LMC from the first 3 MACHO events [15] was indeed $\tau = 8.8^{+7}_{-5} \times 10^{-8}$ and the one from the first two EROS events [16] was similar, $\tau = 8.2^{+11}_{-5} \times 10^{-8}$. The typical event durations of a few weeks were also indicative of lens masses in the ballpark of 0.1 $M_\odot$, i.e. in the limit between brown dwarfs and very light main sequence stars. Furthermore, the non observation of short duration events (T less than a few days) by the EROS CCD program and by MACHO set stringent bounds on light lenses ($10^{-7} < m/M_\odot < 10^{-3}$) which could contribute no more than $\sim 25\%$ to the overall halo mass [17].

Although the number of events were few, they were significantly larger than the backgrounds expected from the known stellar populations. For instance, the faint stars in the galactic disc would contribute little to the optical depth towards the LMC, because although the local disc density is an order of magnitude larger than the halo one ($\rho_0^D \simeq 10^{-1} M_\odot/\mathrm{pc}^3$) its scale height is very small ($h \sim$ 100–300 pc). In general, adding an exponential disc like population with local column density Σ leads to an optical depth to the LMC of $\tau^D \sim 10^{-8}(\Sigma/30 M_\odot/\mathrm{pc}^2)(h/300 \text{ pc})$ [18]. The column density in the thin disc is $\sim 50 M_\odot/\mathrm{pc}^2$, of which 20% is in gas. Furthermore taking into account the measured mass function of disc stars it can be shown that a large fraction of τ^D would be due to stars too bright to go undetected [19], and hence the thin disc predicted depth is actually below 10^{-8}.

The Galaxy is also known to have a thicker disc of stars, with $h \simeq 1$ kpc, probably originating from a past merging of a satellite which somehow heated the disc stars. The column density associated to the observed thick disc stars is typically taken as $\Sigma^{TD} \sim 4 M_\odot/\mathrm{pc}^2$, and hence the expected optical depth is tiny ($\sim 0.5 \times 10^{-8}$). However, in ref. [18] it was noticed that the maximum allowed column density consistent with dynamical observations, $\Sigma^{TD}_{max} \simeq 50 M_\odot/\mathrm{pc}^2$, would lead to $\tau \simeq 5 \times 10^{-8}(h/\text{kpc})$, and hence for the scale height adopted there (1.4 kpc) it would already be close to the observed value.

Another known stellar galactic population is the spheroid (or 'stellar halo'), observed through the old metal poor stars at high latitudes and also as high velocity stars nearby (the observed velocity dispersion is $\sigma \simeq 120$ km/s). It was formed in the first Gyrs of the Galaxy lifetime, has probably a slightly flattened spherical shape ($c/a \simeq 0.7$–1)with density profile $r^{-\alpha}$, with $\alpha \simeq$ 2.5–3.5 [20]. The predicted optical depth for this population, adopting $c/a = 1$ and $\alpha = 3.5$, is $\tau^S \simeq 0.3 \times 10^{-8}(\rho_0^S/10^{-4} M_\odot/\mathrm{pc}^3)$. This value would increase by 50% for $\alpha = 2.5$ and decrease by $\sim 25\%$ for $c/a = 0.7$. The spheroid density inferred from star counts, $\rho_0^S \simeq 5 \times 10^{-5} M_\odot/\mathrm{pc}^3$ leads then to a tiny optical depth. However, there have been since many years suggestions that the spheroid density should be larger by an order of magnitude, based on global fits to the galactic rotation curve and other dynamical observations [21]. In these heavy spheroid models the optical depth results $\sim 4 \times 10^{-8}$, and is hence relevant for observations towards the LMC [22].

Another background for LMC searches is that of old neutron stars [23]. These are born in the disc, but they are

believed to acquire large velocities in the supernova explosions producing them and hence move to large distances where they become more efficient lenses. For the typical value $N_{ns} \simeq 2 \times 10^9$ for the number of past galactic core collapse supernovae [24], the resulting optical depth is $\tau^{NS} \simeq 0.4 \times 10^{-8}$, comparable to the one from known stars in the spheroid or thick disc. If the number of past supernovae were larger. this contribution would increase accordingly.

Regarding the LMC populations, in the same way as the Milky Way has a dark halo, the rotation curve of the LMC suggests that this galaxy also has a dark halo around it. The optical depth associated to it amounts to $\sim 8 \times 10^{-8}$ [25, 26]. Hence, if all the dark matter were in MACHOs the total optical depth would be 20% higher than the prediction from the Milky Way halo alone, and this clearly worsens the discrepancies with the observations. It has to be stressed that no stellar population has been observed with the expected LMC halo distribution. The predictions for the observed distributions of LMC stars (disc and bar) are more delicate. It was actually suggested that the optical depth towards the central bar could be $\sim 5 \times 10^{-8}$ [27], and hence of the order of the observed τ. However, outside the bar, where several of the observed events actually are, τ falls significantly, and the most recent estimates for the expected average depth [28] are $\tau \simeq 2.4 \times 10^{-8}$, although with some spread among different models.

Summarizing, the expectations from known stellar populations amount to $\tau \simeq 3$–4×10^{-8}, while from the Milky Way and LMC halos one would expect $\tau \simeq 5 \times 10^{-7}$. The observed value $\sim 8 \times 10^{-8}$ was clearly larger than the first one, but only a small fraction of the second. Since the main purpose of the microlensing searches was to establish whether the halo consisted of MACHOs, the results are most commonly presented in terms of the fraction f of the Milky Way halo in the form of compact objects, which for the observed τ would correspond to $f \simeq 20\%$. The remaining fraction could be just in cold gas clouds or in non-baryonic dark matter. An alternative explanation was to have instead a heavy spheroid or thick disc made mainly of MACHOs or a very large LMC self-lensing contribution, and instead a completely non-baryonic halo.

Regarding the searches of microlensing of stars in the bulge of the Galaxy, the MACHO, OGLE and DUO collaborations found many events (several hundreds by now) with some being particularly spectacular, as that in fig. 18.15. The high optical depth which is inferred is believed to be due to the barred shape of the inner bulge.

18.5.3 The second period (1996-2000)

In 1996, the results of the analysis of the first two years of MACHO data towards the LMC were announced [29]. A total of 8 candidate events were observed and the average event duration turned out to be longer. The conclusion was that now $\tau = 2.9^{+1.4}_{-0.9} \times 10^{-7}$ and also that the typical lens masses increased to $m \simeq 0.5 M_\odot$. The picture which emerged then was that 50% of the halo should be in objects with the characteristic mass of a white dwarf. This scenario was quite unexpected, and was shown to be also potentially in trouble with the chemical enrichment of the galaxy due to all the metal pollution which would result from the white dwarf progenitors [30, 31]. There were also attempts to explain the observed rates as due to some tidal debris of the LMC or even due to a previously undetected satellite galaxy along the l.o.s. to the LMC [32], but it is not clear whether these ideas are actually supported by observations [33, 34, 35, 36].

In the period after 1996 significant improvements on the observational programs took place: the EROS and OGLE collaborations started to use better cameras in new telescopes and networks of telescopes were organized to follow ongoing alerted microlensing events (GMAN, MOA, PLANET, MPS). This allowed for instance to measure in great detail an event in the Small Magellanic Cloud caused by a binary lens [37] (see fig. 18.16).

When the lens is a binary, the signatures are quite different from the single lens case. For large impact parameters there are now three images of the source, one on the exterior side of each of the lenses and the third one in between

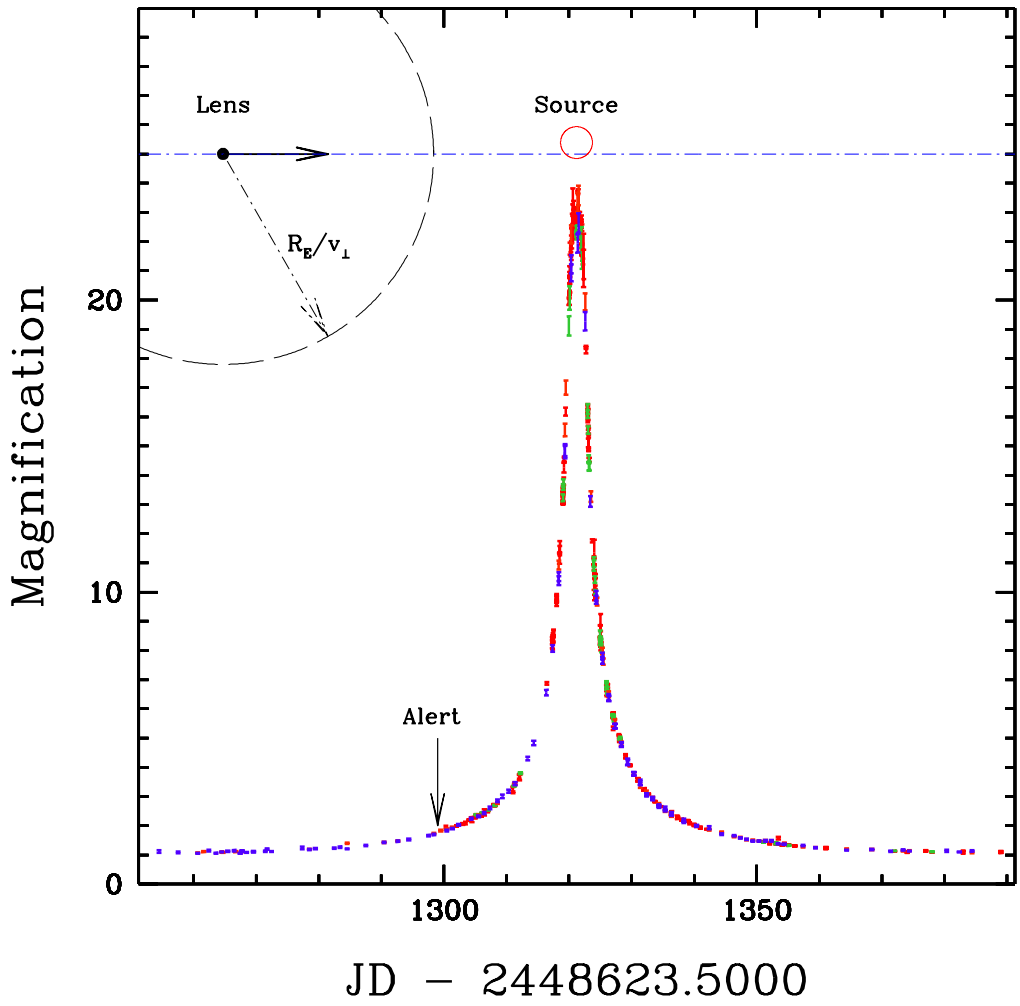

Figure 18.15: Very high magnification microlensing event of a source in the bulge of the Galaxy, seen by MACHO and followed up by several other telescopes. The impact parameter of the lens is actually smaller than the source radius, as depicted in the diagram, and hence effects due to the finite size of the source are observed near the peak.

the lenses. An extra pair of images can appear however for small impact parameters when the source crosses the so called caustic, and then two images disappear again when the source leaves the region delimited by the caustic, as illustrated in fig. 18.17. At these caustic crossings the magnification formally diverges. This means that one has an extremely powerful magnifying glass to look at the source. Actually, effects associated to the finite size of the source become observable and in particular they limit the maximum amplification to a finite value. If one knows the radius of the source, one can also infer the relative lens-source proper motion μ, and since this quantity is expected to differ significantly for lenses in the Magellanic Clouds ($\mu \sim 1$ km/s/kpc) or in the galactic populations ($\mu \geq 10$ km/s/kpc), it was possible to establish that the binary lens belonged to the SMC and not to the halo. Also one of the MACHO LMC events was a binary and its proper motion again suggested that it belonged to the LMC. This shows that indeed the contribution of the lenses in the Magellanic Clouds is significant, and actually in the SMC it is expected to be relatively larger than in the LMC due to the elongated shape of the SMC along the l.o.s..

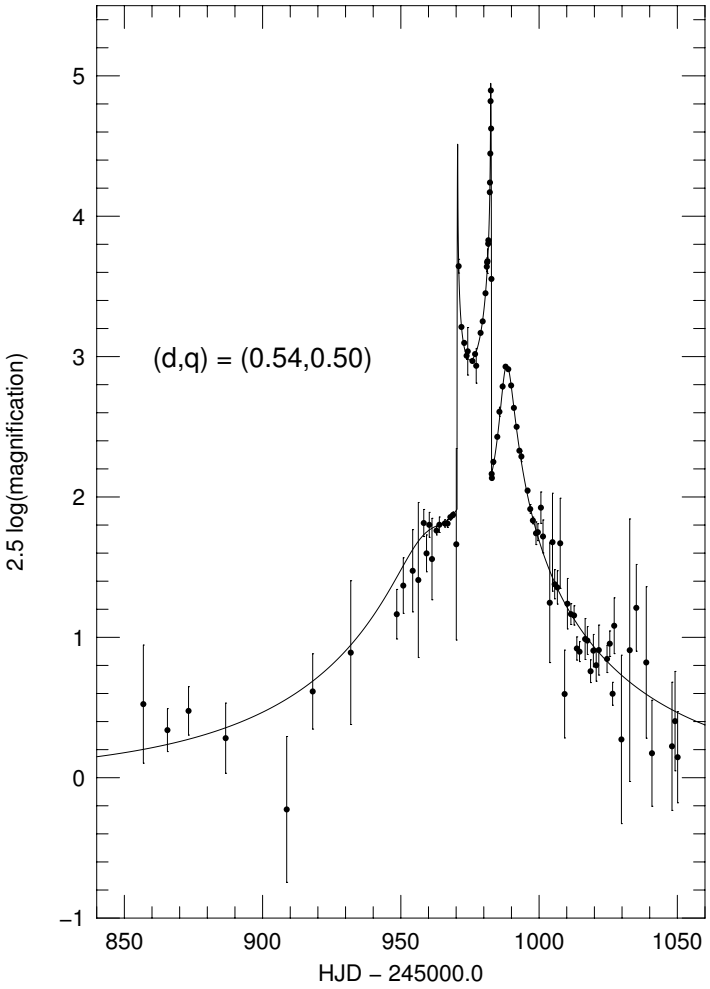

Figure 18.16: Binary event in a source in the SMC. The source finite size effects can be measured during the caustic crossing and indicate that the lens belongs to the SMC.

18.5.4 Recent developments

The most recent microlensing results appeared a few months ago and again changed the overall picture. The analysis of 5.7 yrs of MACHO data [19] in 30 fields (out of a total of 82) found 13–17 events (depending on the criteria used), leading to a significantly reduced depth $\tau = 1.1^{+0.4}_{-0.3} \times 10^{-7}$ (for the 13 event sample). Another relevant observation was that no particular increase in τ towards the center of the Cloud was observed, contrary to the expectations from a rate dominated by LMC stars. Also the EROS group presented the reanalysis of their old data together with two new years of EROS II data [38], finding a total of only 4 events, a result inconsistent with the '96 MACHO result (see fig. 18.18). This shifted the situation somehow back to the initial stage in which the observed rates are a factor $\sim$ 5 below the halo predictions but $\sim$ 3–4 above the expectations from known

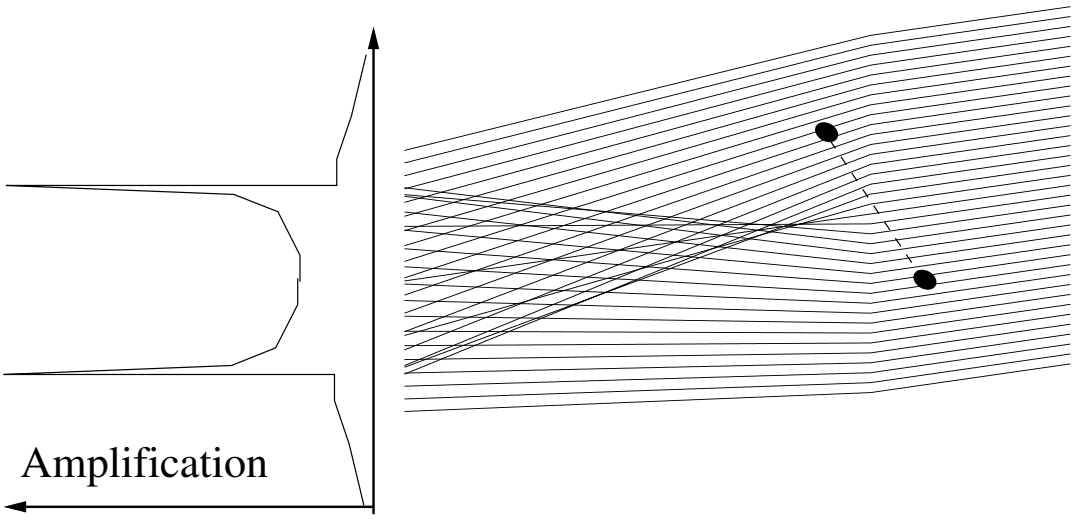

Figure 18.17: Trajectories of the light rays in the mid-plane of a symmetric binary lens. In the turn-off points the magnification becomes divergent, leading to the qualitative light-curve depicted on the left (compare with the previous figure).

populations. The inferred masses $m \simeq 0.5 M_\odot$ continue to suggest however that the objects could be old white dwarfs.

Another important related result has been the recent activity related to the direct search of old white dwarfs. Hansen [39] realized that the spectra of old white dwarfs having molecular hydrogen atmospheres (i.e. probably half of the total) would look much bluer and brighter than previously believed due to the strong absorption at wavelength larger than 1 μm by their atmospheres. This prediction was actually confirmed by the direct measurement of the spectrum of a cool ($T \simeq 3800$ °K) nearby white dwarf [40]. With this new scenario the search for old white dwarfs becomes feasible, and indeed analyses of two Hubble Deep Fields taken two years apart were done searching for objects with large proper motions [41]. The candidate objects they found, with colours consistent with being old 'halo' white dwarfs, led them to infer that their density could be comparable to the local halo density ($\sim 10^{-2} M_\odot/\mathrm{pc}^3$). However, recently two new searches in larger nearby volumes (not so deep but wider) have found results inconsistent with such large white dwarf densities. Flynn et al. [42] found no candidates while expecting a few tens based on ref. [41], while Ibata et al. found two nearby white dwarfs [43], inferring a density of $\sim 7 \times 10^{-4} M_\odot/\mathrm{pc}^3$ for these hydrogen atmosphere white dwarfs. A remarkable thing is that this value is just in the required range to account for the missing mass of the heavy spheroid models, whose proper motions would be only $\sim 20\%$ smaller than those assumed for 'dark halo' objects and hence consistent with those found. To analyse the possibility that these old white dwarfs are genetically related to the old population II spheroid stars, and not to an independent halo population with no observed counterpart, seems then particularly relevant. If this were the case, the initial mass function of spheroid stars would have to be peaked at a few solar masses to account for the large number of white dwarf progenitors, and the gas released during the ejection of their envelopes would have ended up in the disc and bulge, but producing certainly less metal pollution than the halo white dwarf models due to the much smaller total spheroid mass. The future searches of white dwarfs should also be able to distinguish between thick disc and spheroid/halo populations due to their significantly different proper motions.

Regarding the future of microlensing observations, the MACHO experiment has finished taking data, while EROS II and OGLE II are still running. A significant increase in the number of events is then expected when all the data available gets analysed. Furthermore, a new analysis technique (Difference Image Analysis), devised for the study of lensing in crowded fields such as the Andromeda galaxy, has been successfully applied to several bulge fields

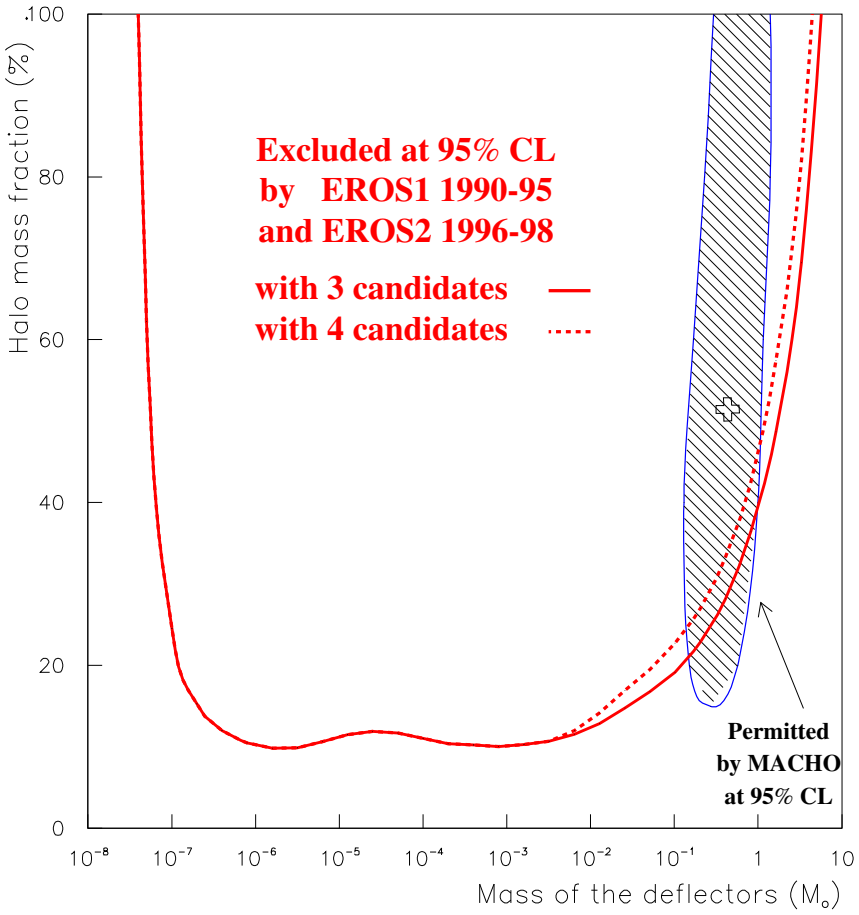

Figure 18.18: Exclusion plot from EROS2 and previous MACHO allowed region.

by the MACHO group [44], doubling the number of observed events with respect to previous analyses, and also by EROS to their first CCD data [45]. The use of this technique for all the LMC data should then also help to get more decent statistics and hence to discriminate among the population(s) responsible for the microlensing events. Clearly the possibility that the dark halo is completely made of non-baryonic dark matter still remains open, and hence the search for its even more elusive constituents is crucial to finally unravel the dark matter mystery.

Chapter

19

Magnetic lensing of UHE cosmic rays

19.1 The cosmic ray puzzles

The cosmic rays (CRs) are very energetic particles which arrive to us from faraway sources. When they hit the upper atmosphere, they produce cascades of secondary particles, which are the ones that are observed on the surface of the Earth. The primaries can be detected by flying detectors into satellites or balloons, but at CR energies above 10^{15} eV the fluxes become too low ($< 1/\mathrm{m}^2\,\mathrm{yr}$) to give significant numbers of events. Fortunately, above these energies the secondary particles in the atmospheric showers start to reach the ground (first in mountain tops at $E \sim 10^{16}$ eV, but at lower altitudes for higher energies) and hence CRs can be indirectly detected by measuring the shower properties in the ground. Another technique to measure energetic showers is to observe the fluorescent light emitted by the nitrogen molecules excited by the charged particles in the shower, what allows to study the longitudinal development of the cascade. The measured spectrum of the cosmic rays arriving to the Earth has the overall shape of a leg, with a knee at 10^{16} eV beyond which it becomes steeper and an ankle at $\sim 5 \times 10^{18}$ eV where it becomes harder again up to the highest energies observed of 3×10^{20} eV, as shown in Fig. 19.1. The region beyond the ankle, i.e. the foot of the spectrum, is attracting renewed interest nowadays with the deployment of large detectors, such as HiRes and Auger, which are expected to find an answer to several issues raised by the observation of such ultra high energy (UHE) events. These are:

i) We don't know the nature of the primaries, i.e. whether they are protons, nuclei, γ rays, neutrinos with new interactions or more exotic objects.

ii) We don't understand the production mechanism giving rise to such enormous energies. Possible scenarios include the stochastic Fermi acceleration in relativistic shocks in magnetic media, electrostatic one-shot acceleration in the electric potential generated by fastly rotating pulsars (these two so-called bottom-up mechanisms have difficulties in reaching energies above 10^{20} eV in view of the size and the magnetic fields known to be present in possible acceleration sites). Alternatively, top-down scenarios have been proposed, such as cosmic ray production in decays of topological defects or of heavy relics from the big bang, but these scenarios remain highly speculative and tend to predict a flux dominated by γ rays and neutrinos, which is not favoured by observations.

iii) We don't know how they manage to propagate from their sources up to us without being attenuated by the cosmic background photons. This is so because if cosmic rays are for instance protons, at energies above 10^{20} eV the relativistic boosts involved are enormous, i.e. $\gamma = E/mc^2 \geq 10^{11}$, and hence the cosmic 3°K microwave photons would be seen in the proton rest frame as gamma rays with energies exceeding 100 MeV. This means that they can produce pions (e.g. exciting the Δ resonance through $p + \gamma \to \Delta \to \pi + p$), and these processes would degrade the cosmic ray energy until it falls below the pion production threshold, corresponding to the Greisen Zatsepin Kuzmin cutoff $E_{GZK} \simeq 5 \times 10^{19}$ eV. This would happen after traversing distances of the order of 50 Mpc [46]. Similarly, nuclei can photodisintegrate through interactions with CMB and IR photons [47] emitting nucleons and hence arriving as lighter (less energetic) fragments. Through these processes, all 'hadronic' CRs with energies above 10^{20} eV would loose their energy in a few tens of Mpc. This should lead to the famous GZK cutoff, which was expected if the sources are indeed cosmological, but that was however not observed in the CR spectrum.

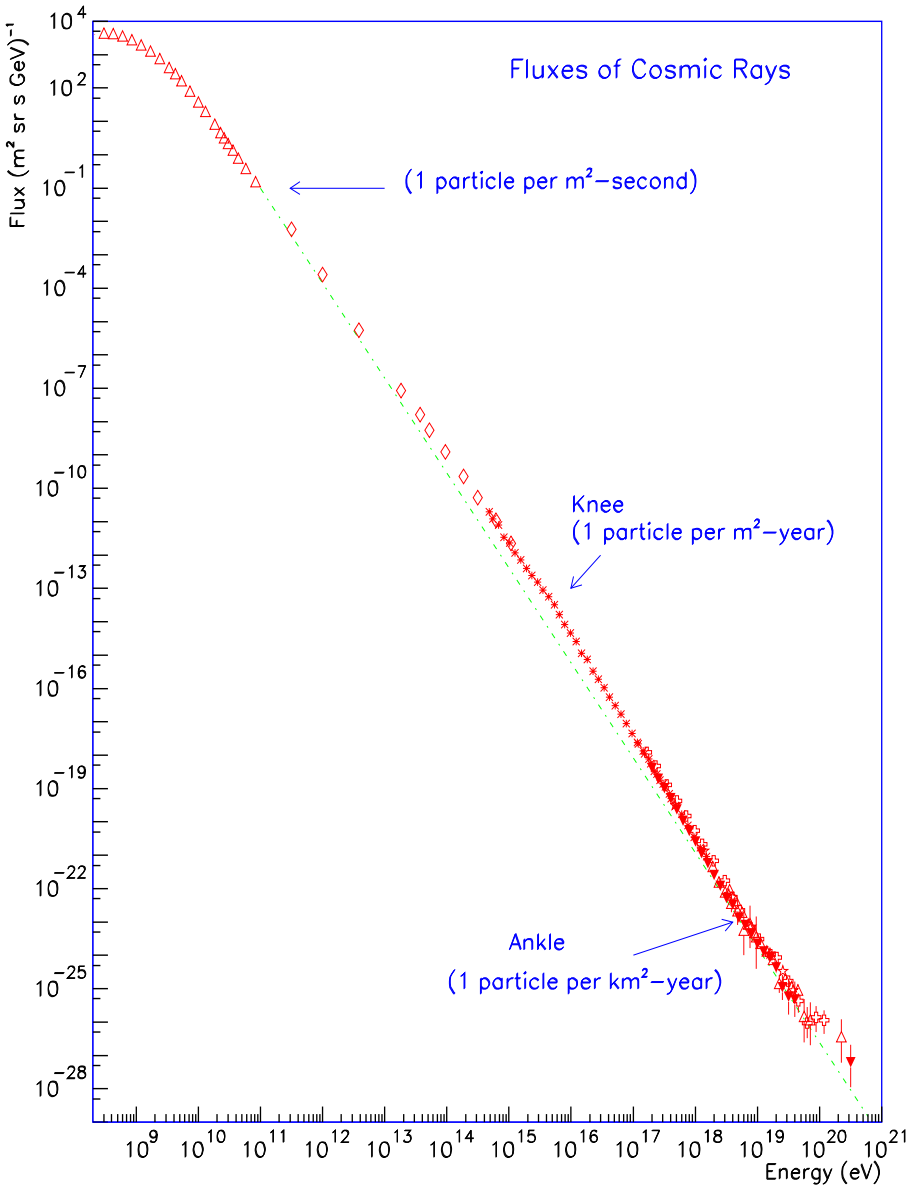

Figure 19.1: Measured cosmic ray spectrum.

iv) We don't know where the sources are located, i.e. if CRs are produced in the Galaxy, if they are extragalactic (e.g. produced in active galaxies or gamma ray bursts) or uniformly spread through cosmological distances, as predicted in some topological defect models.

It is widely believed that below the ankle CRs are protons or nuclei mostly of galactic origin. Since the gyroradius of a CR with energy E and charge Z in a magnetic field B is $R \sim \mathrm{kpc}(\mu G/B)(E/Z\ 10^{18}\mathrm{eV})$, below the ankle the CR trajectories are very curly for the galactic fields of a few μG which are known to exist from Faraday rotation measures (and which tend to follow the spiral structure of the Galaxy) and one has to describe the propagation in terms of diffusion and drift. However, above the ankle the gyroradii become comparable or larger than the scale of the galactic magnetic field, so that trajectories are straighter and one can start to speak of small CR deflections due

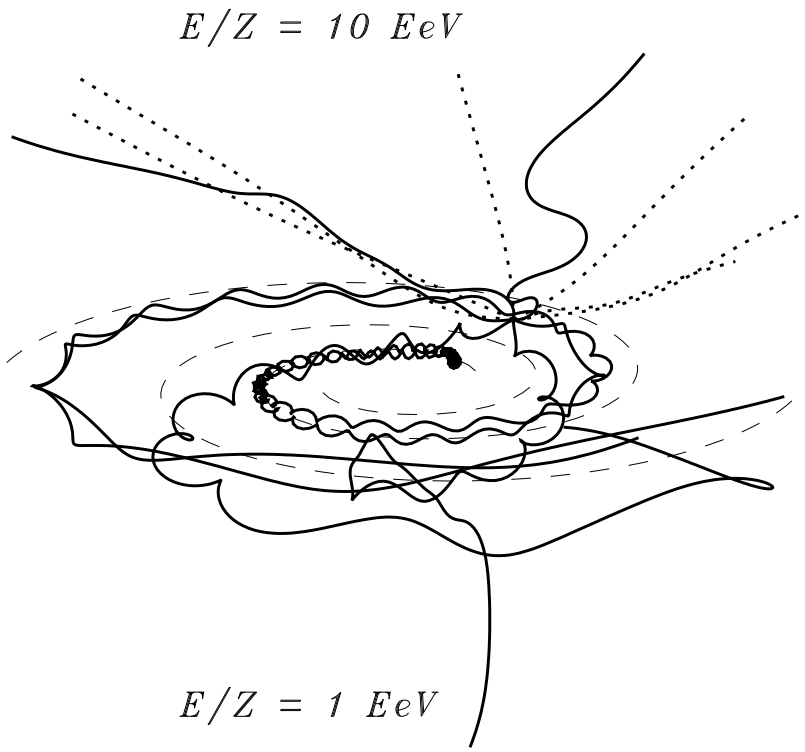

Figure 19.2: Examples of trajectories of nuclei with $E/Z = 1$ EeV ($= 10^{18}$ eV) and 10 EeV. At the lower energies particles start to be trapped by the spiral structure of the regular galactic magnetic field.

to the magnetic fields (see fig. 19.2). In particular one expects to be able to roughly trace back the location of the sources, and hence to do astronomy, with the highest energy events.

The lack of any obvious observed anisotropy towards the galactic plane then suggests that in the 'foot' of the spectrum the CRs are most likely extragalactic. In this case, if CRs are indeed normal hadronic matter (nuclei or protons) the sources of the highest energy events should not be too far, i.e. at less than 20-50 Mpc. Correlations of the observed arrival directions with the location of candidate sources or with the general direction of the supergalactic plane have been searched for, but with no clear evidence of correlations found yet however. The observed spectrum is indeed consistent with an isotropic distribution, with the possible exception of some small scale clustering associated to some observed doublets and triplets of events coming from the same directions in the sky (Fig. 19.3).

When looking for the source locations it is important to correct for possible magnetic deflections using plausible models of the Galactic magnetic fields [49, 50], and eventually also of extragalactic ones if these were to turn out to be very large [51]. For instance, fig. 19.4 shows the directions of arrival to the halo of the highest energy events recorded by AGASA assuming different CR compositions, from protons up to Fe nuclei, adopting a bisymmetric spiral model for the galactic magnetic field [50]. Clearly the deflections are sizeable even at these energies if CRs are heavy nuclei. To do detailed CR astronomy would require then to know the CR composition to some extent.

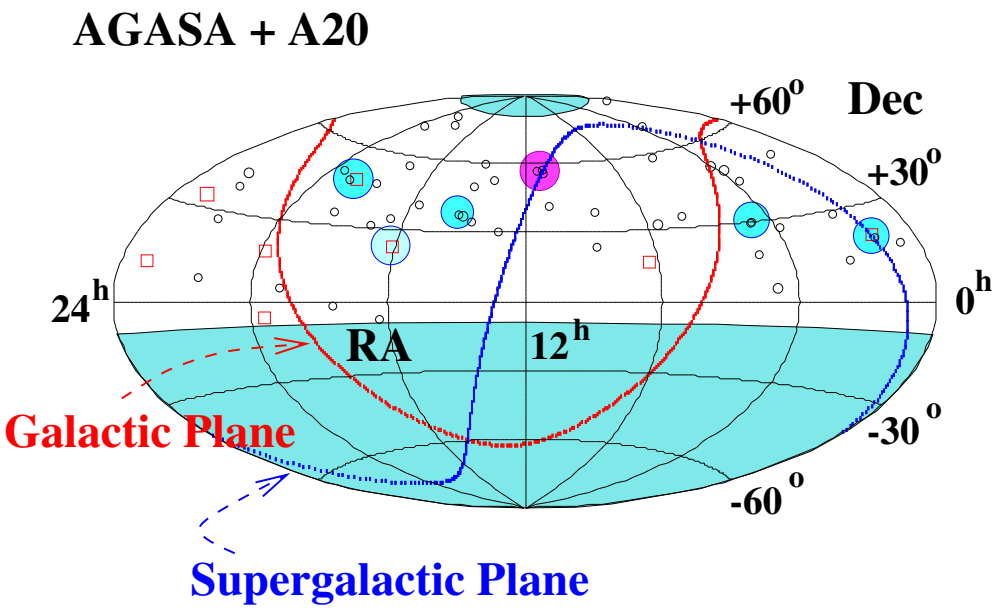

Figure 19.3: Measured arrival directions of the AGASA events with $E > 4 \times 10^{19}$ eV in equatorial coordinates [48]. Events with $E > 10^{20}$ eV are indicated with squares. The big circles indicate the location of doublets and triplets.

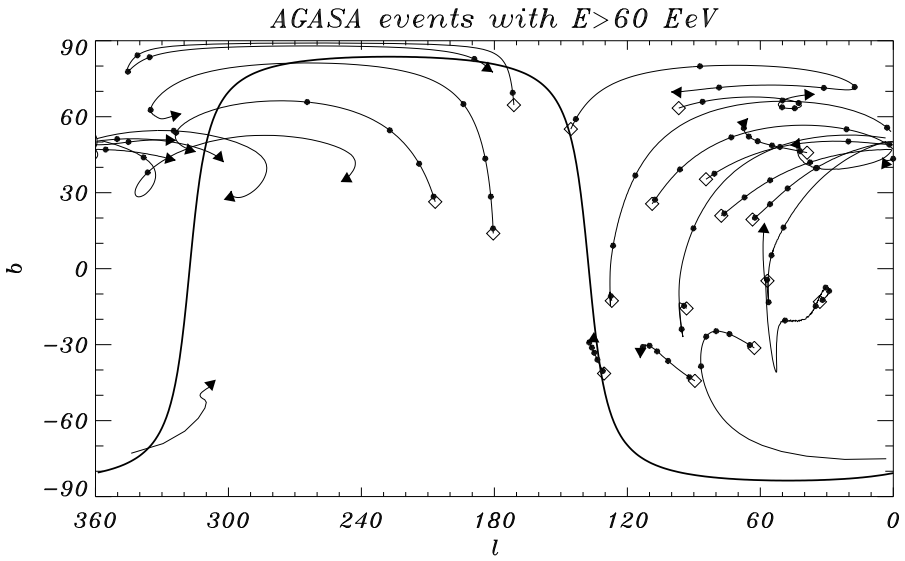

Figure 19.4: Observed arrival directions (diamonds) of AGASA events with energies $> 6 \times 10^{19}$ eV and the corresponding incoming directions outside the Galaxy for different CR charge Z. The dots along the lines indicate the results for $Z = 1, 6, 10, 14$ and 20 and the tip of the arrow is for $Z = 26$ (iron).

19.2 Magnetic lensing effects

As we have shown in refs. [50, 52], magnetic deflections produce other important effects which are even more striking. Indeed, the galactic magnetic field acts as a giant lens and can magnify sizeably the CR fluxes coming

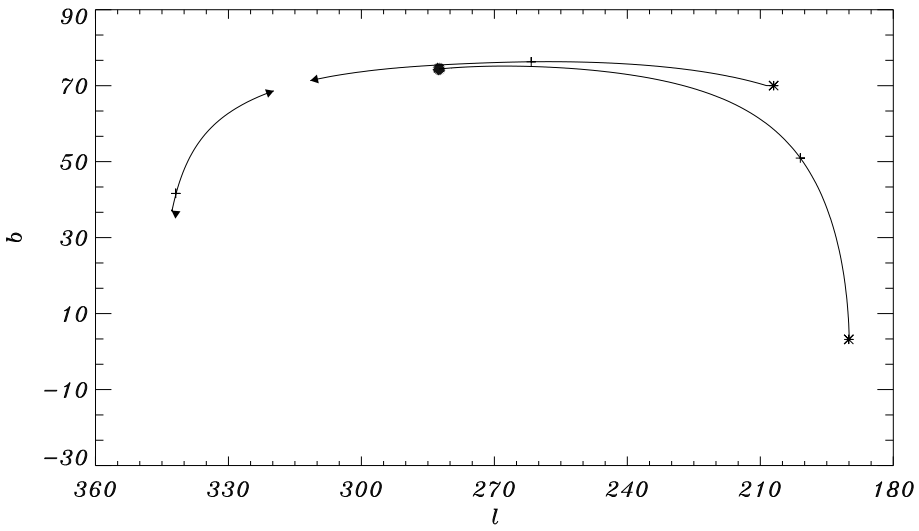

Figure 19.5: Illustration of the angular displacement of the image of a source with energy and of the formation of secondary images in pairs. The actual source (big dot) is in the direction of M87. The secondary images appear where the two arrows meet. The images are located at the plus signs for $E/Z = 10^{19}$ eV and at the asterisks for $E/Z = 5 \times 10^{18}$ eV.

from any given source. Since the deflections are energy dependent, this lensing effect will modify the original spectrum of the source. Furthermore, since the B fields are not homogeneous, CRs from one source may arrive, for a given energy, through more than one path, i.e. multiple images of a source can be seen, in complete analogy with the strong gravitational lensing discussed before. Fig. 19.5 shows an example of multiple imaging of a cosmic ray source assumed to be in the direction of M87 (an active galaxy in the Virgo cluster which is a good potential candidate for acceleration to ultra high energies). The new images appear in pairs (of opposite parity) along critical lines in the sky seen on Earth, corresponding to caustic lines in the source sky. When the source is on a caustic, the magnification of the new pair of images is divergent, but for decreasing energies the caustic moves away from the source and the magnification behaves as

$$\mu_i \simeq A/\sqrt{1 - E/E_0} \pm B \tag{19.1}$$

near the energy E_0 at which the pair of images appeared [52], as shown in fig. 19.6.

When convoluted with a continuous energy spectrum the divergence at the caustic is smoothed out, but anyhow the large magnifications achieved make it more likely to detect events at those energies. This may be helpful to account for some of the doublets and triplets which have been observed, which actually tend to be very close in energy as would be expected from clustering near a caustic.

Notice that for the magnetic field considered, multiple images and lensing effects appear for $E/Z \leq \text{few} \times 10^{19}$ eV (depending on the location of the source). Hence, these effects can be relevant at the highest energies if there is a CR component which is not light. Also, there have been works [53] suggesting that the Galaxy could have a large scale magnetic field extending up to ~ 1 Mpc, associated to a galactic wind, and in this case the lensing effects are present even for protons above 10^{20} eV [54].

There are many analogies [50, 52] between the features of magnetic lensing and the more established gravitational lensing effect. This last is of course achromatic, so that instead of changing the energy as in our discussion above the analog would be to displace the source. For instance, the analog of Eq. (19.1) is the dependence of the magnification of a source in GL with the distance β between the source and a caustic, which is $A \propto 1/\sqrt{\beta}$.

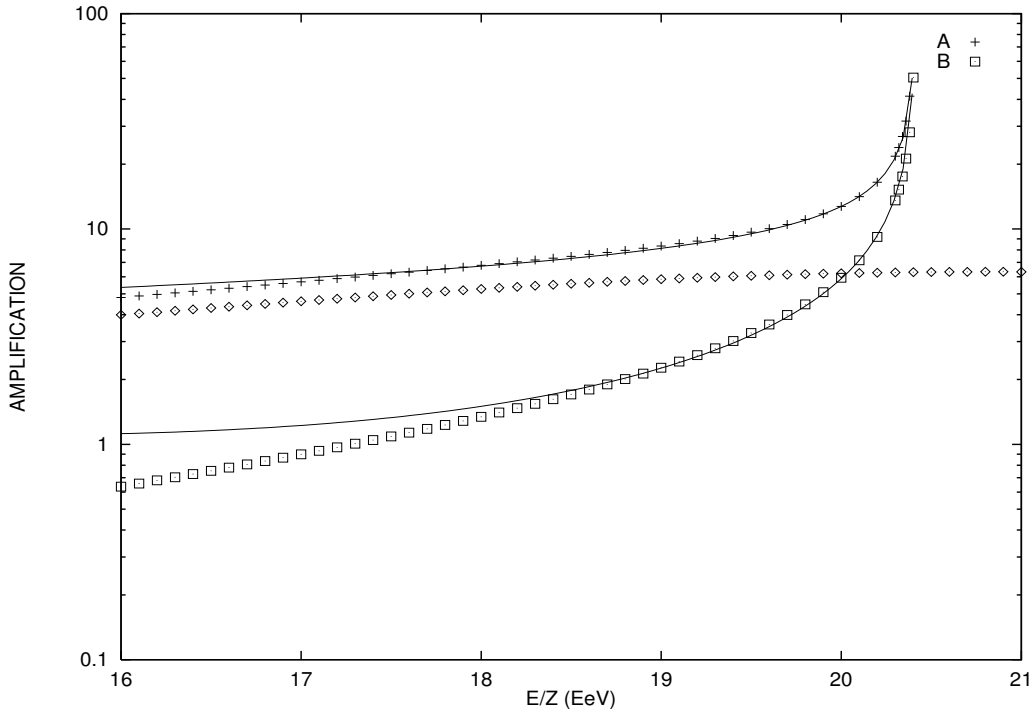

Figure 19.6: Numerical results and analytic fits to the magnification of the CR flux near a caustic, where two images appear, together with the original image (diamonds), for a source located in the direction of M87 in the Virgo Cluster.

Significant time delays also result from the deflections. and they can be relevant for the observation of bursting sources. The lensing effect can also modify the average composition of CRs arriving to the Earth, since for a given energy the magnification of the fluxes depends on the charge of the CR nuclei.

All these effects are important if the ultra high energy CR sky is dominated by a few powerful sources, as would be expected in AGN models. If the CR flux were instead approximately isotropic (as happens at lower energies), the Liouville theorem [55] would preclude the observation of any lensing effect: when a region of the sky is magnified, it is also seen through a larger solid angle and the flux per unit solid angle remains constant. Remarkably, the transition from one regime to the other seems to be precisely around the ankle of the CR spectrum. Hence, a host of interesting effects may be studied with the expected increase in statistics at the end of the CR spectrum to be obtained with the new generation detectors.

Acknowledgments

This work was supported by CONICET, ANPCyT and Fundación Antorchas, Argentina.

Bibliography

[1] K. Olive, G. Steigman and T. P. Walker, astro-ph/9905320.

[2] P. Schneider, J. Ehlers and E. Falco, 1992, *Gravitational Lenses*, (Berlin: Springer Verlag).

[3] R. Narayan and M. Bartelmann, *Lectures on Gravitational Lensing*, astro-ph/9606001.

[4] W. N. Colley, E. Turner and J. A. Tyson, ApJ **461** (1996) 83.

[5] Tyson, J. A., Kochansky G. P., dell'Antonio I. P., ApJ **498** (1998) L107.

[6] N. Kaiser and G. Squires, ApJ **404** (1993) 441.

[7] D. Wittman et al., Nature **405** (2000) 143.

[8] R. Barkana et al., ApJ **520** (1999) 479.

[9] T. Kundic et al., ApJ **482** (1997) 75.

[10] S. Refsdal, MNRAS **128** (1964) 307.

[11] G. Bernstein and P. Fischer, Astron. J. **118** (1999) 14.

[12] E. Roulet and S. Mollerach, Phys. Rep. **279** (1997) 68.

[13] B. Paczynski, ARAA **34** (1996) 419.

[14] B. Paczynski, ApJ **304** (1986) 1.

[15] C. Alcock et al., ApJ **461** (1996) 84.

[16] C. Renault et al., A& A **324** (1997) L69.

[17] C. Alcock et al., ApJ **499** (1998) L9.

[18] A. Gould, J. Miralda-Escudé and J. N. Bahcall, ApJ **423** (1994) L105.

[19] C. Alcock et al., astro-ph/0001272.

[20] A. C. Robin, C. Reylé and M. Crézé, astro-ph/0004109.

[21] J. P. Ostriker and J. A. R. Caldwell, in *Dynamics and structure of the Milky Way*, Eds. W. L. H. Shuter (Reidel, Dortrecht, 1982); K. Rohlfs and J. Kreitschmann, A& A **201** (1988) 51.

[22] G. F. Giudice, S. Mollerach and E. Roulet, Phys. Rev. **D50** (1994) 2406.

[23] S. Mollerach and E. Roulet, ApJ **479** (1997) 147.

[24] F. X. Timmes, S. E. Woosley and T. A. Weaver, ApJ **457** (1996) 834.

[25] A. Gould, ApJ **404** (1993) 451.

[26] X. P. Wu, ApJ **435** (1994) 66.

[27] K. C. Sahu, Nature **370** (1994) 275.

[28] G. Gyuk, N. Dalal and K. Griest, astro-ph/9907338.

[29] C. Alcock et al., ApJ **486** (1997) 697.

[30] B. K. Gibson and J. R. Mould, ApJ **482** (1997) 98.

[31] B. Fields, K. Freese and D. Graff, New Astronomy **3** (1998) 347.

[32] H. S. Zhao, MNRAS **294** (1998) 139.

[33] C. Alcock et al., ApJ (1997) L59.

[34] J. P. Beaulieu and P. D. Sackett, AJ **116** (1998) 209.

[35] D. Zaritsky et al., AJ **117** (1999) 2268.

[36] D. Graff et al., astro-ph/0003260.

[37] C. Afonso et al., astro-ph/9907247.

[38] T. Laserre et al., A& A **355** (2000) L39.

[39] B. M. Hansen, Nature **394** (1998) 860.

[40] S. T. Hodgkin et al., Nature **403** (2000) 57.

[41] R. Ibata et al., astro-ph/9908270; R. A. Méndez and D. Minniti, astro-ph/9908330.

[42] C. Flynn et al., astro-ph/0002264.

[43] R. Ibata et al., astro-ph/0002238.

[44] C. Alcock et al., astro-ph/0002510.

[45] A-L. Melchior et al., A& A **339** (1998) 658.

[46] K. Greisen, *Phys. Rev. Lett.* **16** (1996) 748; G. T. Zatsepin and V. A. Kuzmin, *Sov. Phys. JETP* **4** (1966) 78.

[47] J. L. Puget, F. W. Stecker and J. J. Bredekamp, *Astrophys. J.* **205** (1976) 638; L. N. Epele and E. Roulet, *Phys. Rev. Lett.* **81** (1999) 3295.

[48] H. Hayashida et al., astro-ph/0008102.

[49] T. Stanev, *Astrophys. J.* **479** (1997) 290; G. Medina Tanco, E. Gouveia dal Pino and J. Horvath, *Astrophys. J.* **492** (1998) 200.

[50] D. Harari, S. Mollerach and E. Roulet, *JHEP* **08** (1999) 022.

[51] P. Bhattacharjee and G. Sigl, Phys. Rep. in press, astro-ph/9811011.

[52] D. Harari, S. Mollerach and E. Roulet, JHEP **02** (2000) 035.

[53] E. J. Ahn et al., astro-ph/9911123.

[54] D. Harari,S. Mollerach and E. Roulet, astro-ph/0005483.

[55] G. Lemaître and M. S. Vallarta, *Phys. Rev.* **44** (1933) 224.